THE UNIVERSITY OF CALGARY

AEROTRIANGULATION USING AN

INS-DIFFERENTIAL GPS

by

JAY M. GOLDFARB

A THESIS

SUBMITTED TO THE FACULTY OF GRADUATE STUDIES

IN PARTIAL FULFILLMENT OF THE REQUIREMENTS FOR THE DEGREE

OF MASTER OF SCIENCE IN ENGINEERING

DEPARTMENT OF SURVEYING ENGINEERING

CALGARY, ALBERTA

AUGUST 1987

THE UNIVERSITY OF CALGARY

FACULTY OF GRADUATE STUDIES
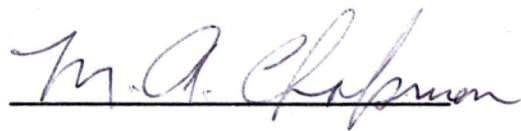
The undersigned certify that they have read, and recommend to the Faculty of Graduate Studies for acceptance, a thesis entitled "Aerotriangulation Using an INS-Differential GPS", submitted by Jay M. Goldfarb in partial fulfillment of the requirements for the degree of Master of Science in Engineering.

Dr. K.P. Schwarz (Supervisor)
Dept. of Surveying Engineering

Dr. E.J. Krakiwsky
Dept. of Surveying Engineering

Prof. M.A. Chapman
Dept. of Surveying Engineering

28 September 1987

Dr. W.H. Dilger
Dept. of Civil Engineering

ii

ABSTRACT

Aerotriangulation is a key step in creating maps from aerial photographs. Conventionally, ground control is provided to relate the photographs to a reference coordinate system. The establishment of ground control, however, is difficult and costly, especially in remote areas. It has been proposed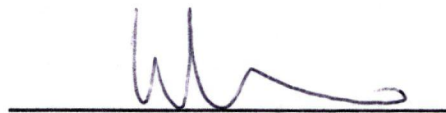 that ground control be replaced by control at flight level (Schwarz et al., 1985). Methods for obtaining precise aircraft positions and for using these positions for aerotriangulation have been investigated in this study. Two positioning strategies are examined. The first combines output from a stable-platform inertial navigation system (INS) with differential Global Positioning System (GPS) pseudoranges. The stable-platform INS output is characterized by a very low random noise level (less than 1 cm/s), but is subject to deterministic errors which grow very large with time. Conversely, differential GPS observations have a higher noise level but the resultant positions are unbiased. The first strategy exploits the complementary characteristics of these observations. An INS error curve is fit to the discrepancies between the raw INS positions and the GPS positions. Estimated corrections to the INS positions are then available for any epoch of interest. The second strategy uses GPS carrier-phase observations, which, if not for the presence of cycle slips, would be of sufficient precision for aerotriangulation. In order to remove the effects of cycle slips, an inexpensive strapdown INS can be used. In both strategies, the INS serves two further purposes: to interpolate positions at the exposure epochs and to monitor the orientations of the offset vectors between the INS reference centre, the GPS antenna phase centre, and the camera's perspective centre. Simulations were carried out to test the proposed positioning strategies. Resulting root-mean-square (rms) coordinate errors were between 0.28 and 0.59 metres for the first strategy, and between 0.08 and 0.36 metres for the second strategy. Photogrammetric simulations were performed to test the applicability of the positions to aerotriangulation. In order to determine the detrimental effects of variations in the primary elements of interior orientation, random perturbations were applied to the camera principal distance and to the principal point offsets. Using a photography scale of 1: 50 000, the resultant rms tie point errors were between 0.47 and 0.69 metres in planimetry and between 1.87 and 2.59 metres in height. These results are sufficient for Class "A" topographic maps at scales up to 1: 50 000. If the principal distance remains constant during the photography, however, the height error is mainly composed of a bias. If this bias can be tolerated, map scales as large as 1: 20 000 may be feasible. Recent results on GPS phase data (Schwarz et al., 1987) have confirmed the simulation results. Aerotriangulation tests are planned.

ACKNOWLEDGEMENTS

TABLE OF CONTENTS

CHAPTER

LIST OF TABLES

LIST OF FIGURES

NOTATION

<u>Key symbols</u>

$\mathbf{A}$	Jacobian (first design) matrix
$\mathbf{C_u}$	covariance matrix of vector $\mathbf{u}$
$\mathbf{dp}$	vector of differences between GPS and INS-derived positions
$_s\mathbf{e}_i$	unit vector from receiver i to satellite s
f	camera principal distance
$\mathbf{f}$	specific force vector
$\mathbf{g}$	gravity vector
$\mathbf{g}^*$	gravitation vector
h	geodetic height
$_s N_{12}$	integer ambiguity in $\Delta_s \phi_{12}$
$\mathbf{r}$	position vector
$\mathbf{R}_w$	rotation about w-axis (direction cosine matrix)
$^j\mathbf{R}_i$	rotation from i system into j system (direction cosine matrix)
$\mathbf{v}$	velocity vector
$\mathbf{w}$	misclosure vector
$^{in}x, {}^{in}y$	photocoordinates in photo n
x_{pp}, y_{pp}	photocoordinates of principal point of minimum variance
$^G x_n, {}^G y_n, {}^G z_n$	perspective center coordinates for photo n
$^i x, {}^i y, {}^i z$	Cartesian coordinates expressed in i system
$\mathbf{y}$	vector of coefficients in INS error model
$\delta\phi, \delta\lambda, \delta h$	INS position errors
$\Delta\mathbf{r}_{12}$	baseline vector from receiver 1 to receiver 2

λ	geodetic longitude
$\Delta_s \rho_{12}$	difference in GPS pseudoranges between recievers 1 and 2 and satellite s
$\Delta_s \phi_{12}$	single-difference phase measurement between receivers 1 and 2 and satellite s
$^s\rho_i$	GPS pseudorange from satellite s to receiver i
ϕ	geodetic latitude
ω_{ie}	earth rotation rate (relative to inertial space)
$\boldsymbol{\omega}_{ie}$	earth rotation vector
ω_s	Schuler rate
$^i\Omega_{ji}$	skew-symmetric matrix of angular velocities of i system relative to j system coordinitized in i system

Matrices are denoted by bold upper-case letters, vectors by bold lower-case letters.

Note: Some symbols may have other meanings in certain contexts, but these cases are clearly identified in the text.

Coordinate systems (superscripts or subscripts)

AC	aircraft
CT	conventional terrestrial
G	local reference system for aerotriangulation
I	operational inertial
LL	local level
RA	right ascension

Operators

$\mathbf{W}^T$	transpose of matrix $\mathbf{W}$
$\mathbf{W}^{-1}$	inverse of matrix $\mathbf{W}$
$\dot{a}, \ddot{a}$	first and second time derivatives of a
$\Delta \bullet$	change in $\bullet$
$\langle \bullet \rangle$	estimate of $\bullet$

Chapter 1

Introduction

Since the middle of this century, virtually all topographic mapping has been done photogrammetrically using aerial photographs. In order to relate two-dimensional photographs to a three-dimensional coordinate system for mapping, control points, i.e. points with known coordinates, are needed. Traditionally, control points are established on the ground using terrestrial surveying methods. The establishment of ground control is difficult and expensive, especially in remote areas. Consequently, a lot of effort has been expended in developing ways to minimize the amount of ground control required.

Major reductions in required control are achieved by using analytical methods in which the relationships of a large number of overlapping photographs to a three-dimensional reference coordinate system are determined simultaneously. Further reductions have been achieved by the use of auxiliary data, primarily from airborne sensors (Blais and Chapman, 1985; Corten, 1984). These methods have not as yet entirely eliminated the need for ground control. The recent development of the NAVSTAR Global Positioning System of satellites (GPS), however, has made precise positioning of an aircraft feasible, and ground control may soon be unnecessary for medium to small-scale photomapping.

Schwarz et. al. (1984) suggested the removal of control to flight level by combining a GPS receiver with an inertial navigation system (INS), and they demonstrated the feasibility of using the derived aircraft positions in a

1

photogrammetric block adjustment. The work done for this thesis is an extension of their original study.

The thesis is divided into three parts. Chapters 2 through 4, which comprise the first part, describe the strategies and mathematical models for aircraft postitioning using an INS-GPS and present results of simulations. Chapters 5 and 6, part two, discuss photogrammetric models and processing, and describe the unique problems which arise when ground control is eliminated. Results of photogrammetric simulations are also presented. In Chapter 7 (part three), conclusions are drawn and recommendations for further study are made.

Chapter 2

Positioning Concepts and Strategies

The objective of this research is to develop methods for determining the precise positions of an aircraft at the times of exposures of aerial photographs and for using these positions as exclusive control in aerotriangulation. As mentioned in the previous chapter, two different types of navigation systems will be used. One system, the inertial navigation system, or INS, has been in existence in some form since the Second World War. The second system, the NAVSTAR Global Positioning System, or GPS, came on the scene much more recently. It is the synergism between these two types of systems which has made the techniques described in this report feasible.

This chapter begins with brief conceptual descriptions of INS and GPS, and ends with an outline of two separate strategies for combining output from these systems to obtain positions having the precision required for aerotriangulation.

2.1 Inertial Navigation Systems (INS)

The operating principle of inertial navigation systems is based on Newton's second law of motion, i.e.

$$\text{force} = \text{mass} \cdot \text{acceleration}.$$

The basic components of an INS are accelerometers and gyroscopes. Usually, three accelerometers are mounted orthogonally to provide measurements of specific

force (force per unit mass) in a Cartesian coordinate system. Two or more gyroscopes are provided to monitor changes in orientation of the accelerometer frame and, in some mechanizations, to maintain a particular reference frame physically by means of a gimballed platform. Starting with information obtained at an initial point, changes in position are obtained by two successive time integrations of the gravity-corrected specific force measurements. The gyroscopes provide data for the coordinate transformations necessary to the process.

Britting (1971) classifies inertial navigation systems as geometric, semianalytic, or analytic. Geometric systems physically maintain, or *instrument*, two separate coordinate frames: an operational inertial coordinate frame and a navigational coordinate frame. The advantage of a geometric INS is that positions are available directly as analog output, thus eliminating the need for a digital computer. For this reason, early INS's were geometric. The analog output, however, is obtained at the price of a good deal of mechanical complexity.

Semianalytic, or stable-platform systems, instrument one reference frame, which may be either inertial or navigational. These systems do require a computer to effect the necessary coordinate transformations. To date stable-platform INS's have been the only type of system used for surveying applications. Two different mechanizations are now in use. In the *space-stable* mechanization the accelerometer platform is maintained in an orientation which is constant with respect to inertial space. This mechanization is not considered in this study. The other type of INS in use for surveying is the *local-level* mechanization. Figure 2.1 is a block diagram of an ideal (errorless) INS of this type. The accelerometers and gyroscopes are mounted on a gimballed platform. The platform is initially aligned by leveling and gyrocompassing at a point of known location. When aligned, the three accelerometer axes point east, north, and up. As the INS is moved, the
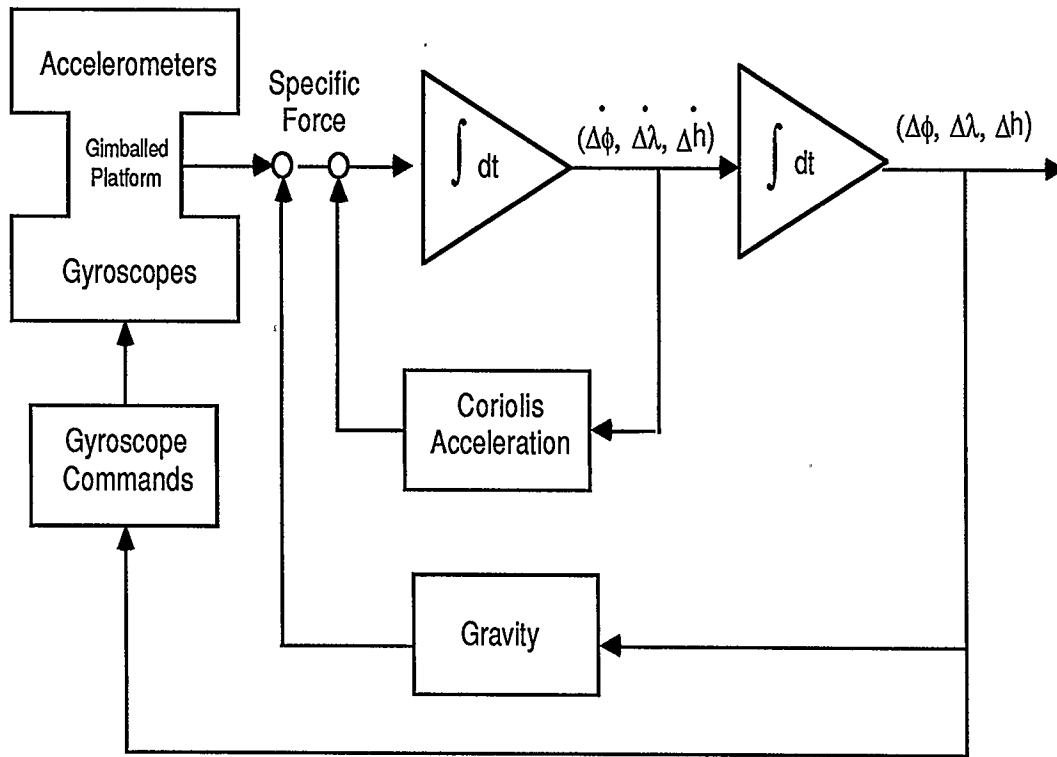
Figure 2.1.   Ideal local-level INS

computer calculates gyroscope torque commands which control the orientation of the platform so that the accelerometers maintain the same directions relative to the ellipsoidal earth model. Specific force measurements are corrected for Coriolis acceleration, which is a function of the velocities (computed from the output of the first integrator), and for gravity, which is a function of position (computed from the output of the second integrator). Note that the constants of integration, initial position and velocity, have been omitted from the figure but are necessary for the computations. The change in the gravity vector induced by the movement of a vehicle is slow compared to the change in Coriolis acceleration. Therefore, the inner (velocity) loop usually operates at a much faster rate than the outer

5

(acceleration) loop, and the mechanization equations are written in terms of velocities, as will be seen in Chapter 3.

In contrast to the other types of systems, the analytic mechanization does not physically instrument a reference frame. The accelerometers and gyroscopes are (except for some damping) rigidly attached to the vehicle which carries the INS. For this reason, analytical systems are most commonly referred to as "strapdown" INS's. Figure 2.2 shows an ideal strapdown INS *mathematically* mechanized in the local level frame. Again, integration constants have been omitted. As shown in the figure, the physical gimbals have in essence been replaced by "analytical gimbals" (VonBronkhorst, 1978). The purpose of the gyroscopes is to supply rotaion rate data for the transformation of the specific forces into the local level system. The vehicle, and hence the accelerometer-gyroscope platform, may change its orientation with respect to inertial and earth-referenced coordinate frames very rapidly. Consequently, time intervals for numerical integration of the system output must be quite short, and a high degree of computer power is necessary to obtain velocities and positions. However, strapdown inertial systems are relatively simple mechanically and are less expensive than other types of systems. Because they have appeared on the scene most recently, the error behaviour of strapdown systems is the least understood of the three types.

The relationships between the three types of inertial navigation systems are illustrated in Figure 2.3.

For the application under consideration, inertial navigation systems have the following desirable characteristics:

1. INS errors are largely deterministic and although system errors can become quite large over time, they are easily managed given some form of external monitoring.

2. System output is obtainable at very short time intervals.

6

As will be seen, these characteristics complement those of GPS very well.
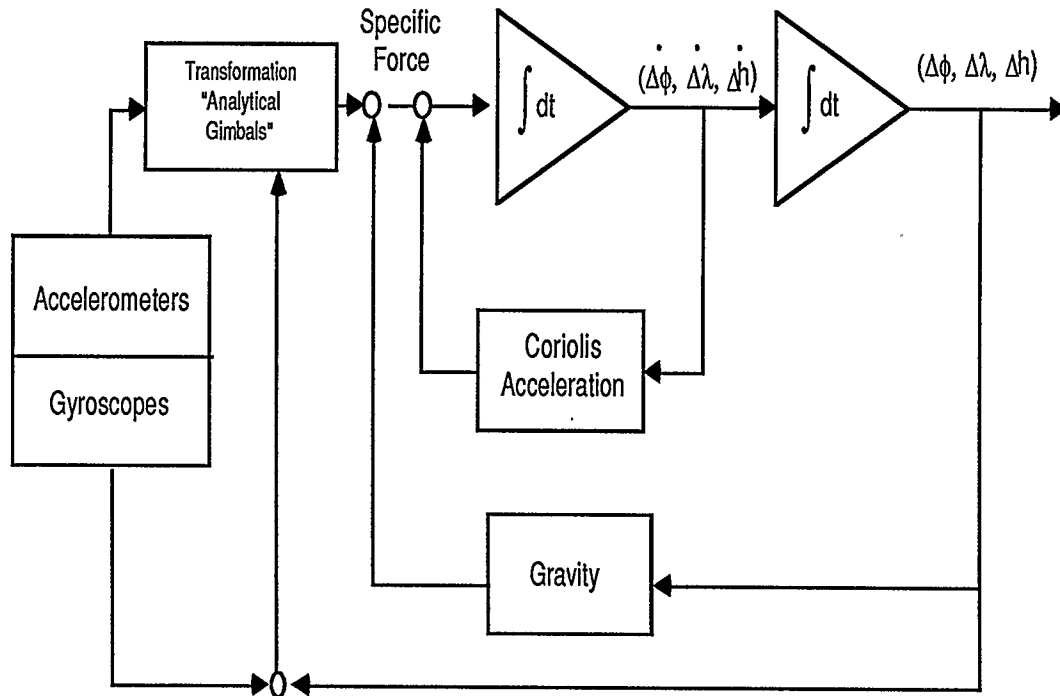
Figure 2.2.   Ideal strapdown INS

INS system errors must be monitored by external observations if they are to remain manageable. For terrestrial surveying, this is most commonly done by a zero-velocity update, or ZUPT. Here, the vehicle carrying the system is stopped for a short time period during which a series of velocity outputs are obtained from the INS. As a first approximation, these velocities are direct measures of the velocity state errors of the system. Obviously, this technique is not practical if the vehicle is a fixed-wing aircraft. Instead, external observations can be obtained from a separate system, such as a barometric altimeter, or, in this case, a GPS receiver.

COMPUTER LOAD

MECHANICAL COMPLEXITY

DEVELOPMENT TREND

GEOMETRIC   SEMIANALYTIC (STABLE PLATFORM)   ANALYTIC (STRAPDOWN)
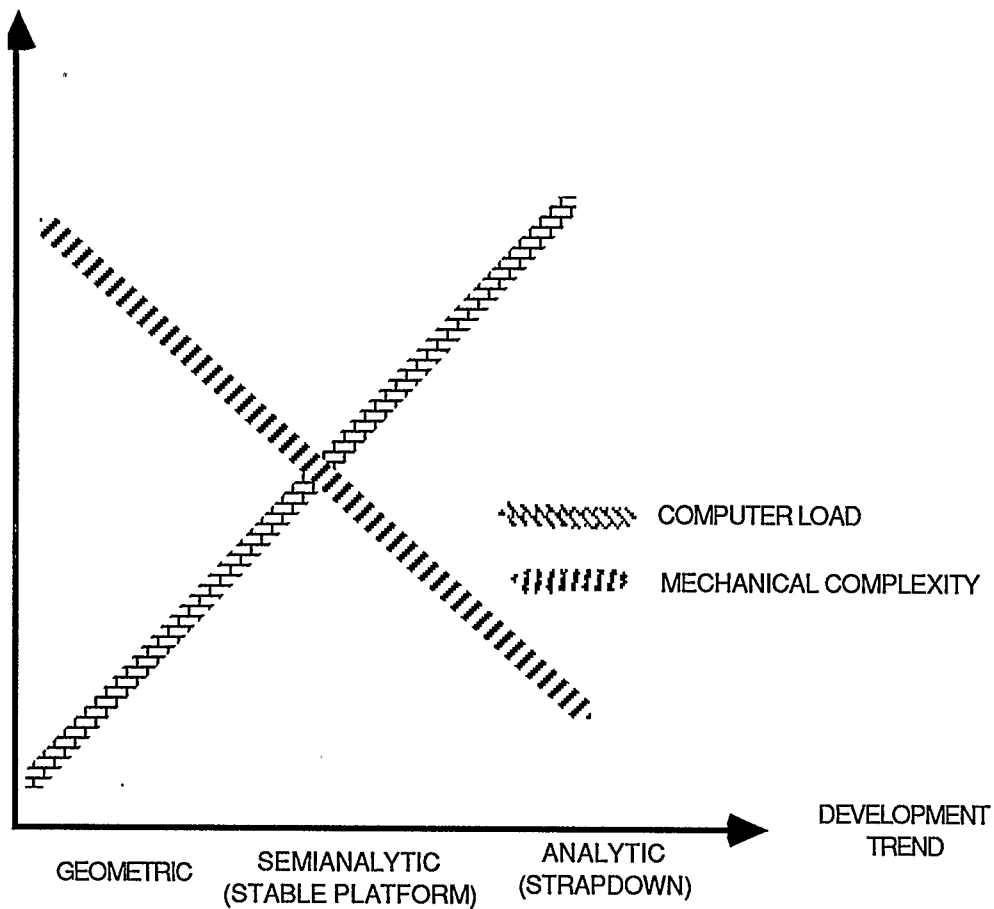
Figure 2.3.   **Relationships between INS types**

2.2 NAVSTAR Global Positioning System

The Global Positioning System was designed by the U.S. Department of Defense (DOD) to provide military users with instantaneous three-dimensional positions having uncertainties of 10-20 metres. When the full satellite constellation is deployed, there will be 18 satellites in six orbital planes plus three active spares (Fullenwider and Jorgensen, 1984). The nominal altitude of the satellites is 20 183 kilometres, yielding a period of approximately 12 hours (Milliken and Zoller, 1980). This constellation will provide navigation coverage worldwide 24 hours a

day. During the development and deployment period, the DOD plans to phase out virtually all of the other navigation systems which it currently supports. Full deployment was originally scheduled for the mid-1980's, but the schedule has been set back by the Challenger disaster.

GPS was designed to provide a means of timing the transit of a radio wave from the satellite to the receiver. The system achieves this by providing a uniform, continuous time frame and by superimposing time marks on the radio signals broadcast by the satellites. The time frame (referred to as GPS time) is established by designating a hydrogen maser clock at one of the tracking stations as the reference standard. Each satellite is equipped with an atomic clock; rubidium clocks were used in the prototypes, but cesium clocks have been used in more recently-launched spacecraft. Hydrogen maser clocks are slated for launch in future vehicles. The behaviour of the satellite clocks is monitored at the tracking stations, and clock correction coefficients are uploaded to the satellites to be included in the broadcast navigation message. Time marks are superimposed on the signals by modulating the broadcast carrier with pseudorandom binary codes.

The satellite clocks have a nominal frequency of 10.23 MHz, which is reduced slightly to correct for relativistic effects. The maximum allowable uncertainty in this clock rate is one part in 10^{12} (Milliken and Zoller, 1980). The manufacture of small, lightweight oscillators of this quality is one of the most important technological achievements in GPS. Each satellite broadcasts at two frequencies, each of which is an integer multiple of the nominal clock frequency: L_1, at 154 times the clock frequency or 1575.42 MHz, and L_2, at at 120 times the clock frequency or 1227.6 MHz. Two frequencies are provided to allow measurement of ionospheric group delay, which is, in part, frequency-dependent (Spilker, 1980).

9

The L_1 signal is given by

$$L_1(t) = A \cdot P(t) \cdot D(t) \cdot \cos(2\pi f_1 t + \theta)$$

$$+ 2A \cdot C(t) \cdot D(t) \cdot \sin(2\pi f_1 t + \theta) \qquad (2.1)$$

where

A is proportional to the signal amplitude,

$P(t)$ is a pseudorandom binary code having a bit rate of 10.23×10^6 bps and a period of approximately 38 weeks (but is reset every week),

$C(t)$ is a pseudorandom binary code having a bit rate of 1.023×10^6 bps and a period of 1×10^{-3} seconds,

$D(t)$ is a 50 bps data stream containing the user navigation message and other pertinent data,

f_1 is the L_1 frequency, and

θ is a small phase noise and oscillator drift component (Spilker, 1980).

The L_2 signal is similar. $P(t)$ is known as the P-code or precise code, while $C(t)$ is known as the C/A-code or clear/access code (Milliken and Zoller, 1980).

The original design of the system calls for the receiver to lock onto the C/A code by cross-correlation of the received signal with a replica of the C/A-modulated signal produced by the receiver. The point of maximum signal correlation is obtained by searching through the 1023 chips in a C/A code period. The C/A code thus acts as a rough vernier. The user has then obtained a coarse estimate of the (biased) range to the satellite, but this estimate is ambiguous because the C/A code has a period of only one millisecond. To resolve this ambiguity, the range must be known with an uncertainty of less than 150 kilometres, which is the distance traveled by light in half a millisecond. Through the navigation message, the user obtains an indicator of the GPS time of broadcast of a particular point in the code

stream. With prior knowledge of the timing of the P-code, an estimate has thus been obtained of the time offset between a replica of the P-code produced in the receiver and the received P-code, which acts as a fine vernier. Because the transit time of the signal from the satellite to the earth is bounded between 67 and 90 milliseconds and the P-code has a period much larger than this, the time offset obtained at the point of maximum cross-correlation between the two P-codes gives an unambiguous (but biased) estimate of the satellite to receiver range. Figures 2.4a and 2.4b illustrate a portion of a pseudorandom binary code and a portion of
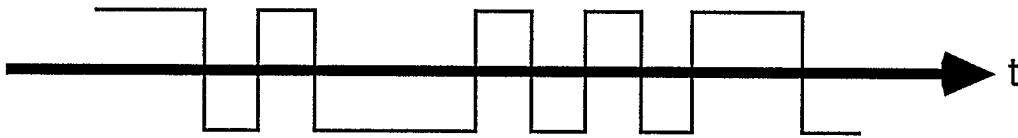
Figure 2.4a.   Pseudorandom code

Figure 2.4b.   Autocorrelation peak

the corresponding autocorrelation function. Peaks in the autocorrelation function for the C/A-code are separated by one millisecond, while peaks for the P-code are separated by 38 weeks. Each satellite is assigned a one-week portion of the P-code.

If the user's clock were in perfect synchronization with the GPS time, range measurements to three satellites would give a unique determination of the receiver's position. In most cases, however, the receiver clock can only be synchronized to

11

GPS time within 100 nanoseconds (Remondi, 1984). This results in a 30 metre range uncertainty and the bias mentioned above. Furthermore, random irregularities are present in the quartz oscillators which are used in most receivers. Therefore, GPS code measurements are commonly called "pseudoranges", and the usual algorithm for instantaneous positioning requires ranges to four satellites for a unique determination of three coordinates and a time offset.

The major sources of error in GPS positioning can be categorized according to their location on the signal path, i.e.:

1. Satellite
   - orbit prediction errors
   - satellitie clock errors

2. Propagation
   - ionospheric group delay uncertainties
   - unmodeled tropospheric delay

3. Receiver
   - multipath effects
   - receiver noise and truncation error

These will be discussed in greater detail in Chapter 3. For now, it is important to note that the first three of these error sources, and to a lesser extent the fourth, are largely eliminated if pseudorange observations are replaced by pseudorange difference observations. These difference observations can be obtained by maintaining a second receiver at a fixed point; this is the so-called *differential* mode of GPS operation. The improvement in performance is due to the fact that satellite and propagation errors are highly correlated at the two receiver sites. Using the differential method, uncertainties in each coordinate can be reduced from 10-20 metres to 5-10 metres. More importantly for this research, differential pseudoranges yield *unbiased* position estimates. The differential technique will be emphasized in the sequel.

In the late 1970's, several radio astronomers, notably Charles Counselman at MIT (Counselman and Shapiro, 1979) and Peter MacDoran at JPL (MacDoran, 1979), began to adapt the techniques of very-long-baseline interferometry (VLBI) to the GPS signal, and found that relative baseline accuracies of one part in 10^{-6} or better could be obtained. These techniques treat the satellite signals as truly random signals and cross-correlate on the *carrier* instead of on the code. Shortly thereafter, researchers with experience in navigation using Doppler observations on the Navy's TRANSIT satellites began to explore the possibility of utilizing the same techniques on the GPS carrier to improve resolution and reduce noise (see, for example, Hatch, 1982). Kinematic tests using these techniques have already yielded precision at the sub-metre level (Mader, 1986; Cannon, 1987). One of the two strategies employed in this research uses carrier-phase observations.

A further motivation for both carrier-phase correlation and for differential utilization of GPS is the DOD's policy of "selective availability". The DOD plans to deny access to the P-code to most non-military users of the system. Further, the DOD will degrade the information provided in the broadcast navigation message so as to limit the attainable instantaneous accuracy available to general users.

2.3 GPS-INS Combination Strategies

There are four basic types of data which will be utilized: positions derived from a stable-platform INS, positions derived from a strapdown INS, positions derived from GPS differential P-code observations, and positions derived from differential GPS carrier-phase observations. Two separate strategies for the combination of these observations will be explored.

The first strategy combines positions obtained from a stable-platform INS with differential GPS P-code observations. This strategy represents a true system

13

integration and can be explained as follows. As mentioned in §2.1, errors in positions derived from an INS are largely deterministic; the noise level of the velocities obtained from a commercially-available stable-platform INS is less than 1 cm s^{-1}. Over time, however, large biases accumulate which must be monitored by an external source in order to be manageable. On the other hand, positions from differential GPS pseudoranges, while of somewhat lower precision (5-10 m), are largely unbiased. Figure 2.5 illustrates these error characteristics schematically. The idea in the first strategy is to fit a curve based on the stable-platform INS error
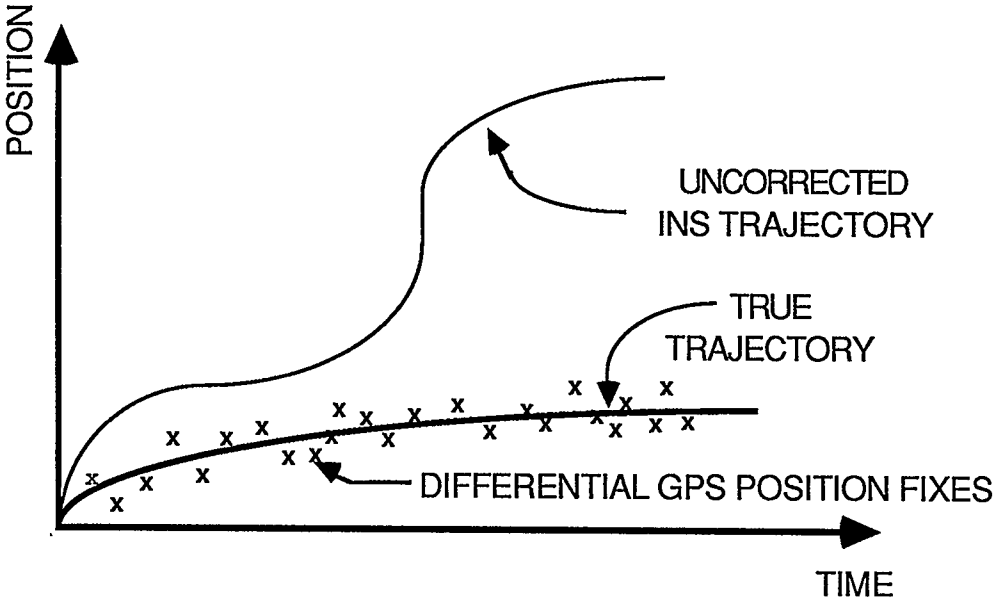
Figure 2.5. **INS-Differential GPS**

model to the differences between positions derived from GPS and positions from the INS. The new differences obtained from the curve fit are then applied as corrections to the raw INS data. In this way, the smoothness of the INS data is preserved, while the GPS differential pseudoranges serve to remove the bias. This is a batch procedure which is summarized in Figure 2.6.

14

```
┌─────────────────┐          ┌─────────────────┐
│ STABLE-PLATFORM │          │ GPS DIFFERENTIAL │
│ INS POSITIONS   │          │ P-CODE POSITIONS │
└─────────────────┘          └─────────────────┘
         │                            │
         │   ┌──────────────────┐     │
         └──▶│ CURVE FIT OF GPS-INS │◀─┘
             │ POSITION DIFFERENCES │
             │ TO INS ERROR MODEL   │
             └──────────────────┘
                      │
                      ▼
             ┌──────────────────┐
             │  POSITIONS w/     │
             │  UNCERTAINTIES    │
             │  < 0.6 M          │
             └──────────────────┘
```
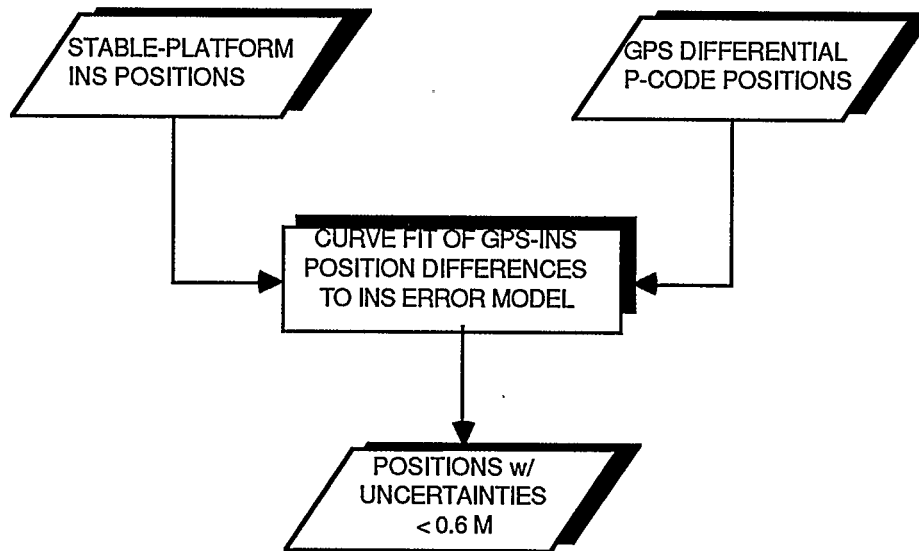
Figure 2.6.   Positioning strategy 1

The second strategy uses GPS differential carrier-phase data as the primary source of positions. By themselves, these positions have the precision required for aerotriangulation, and an INS would be unnecessary if GPS receivers functioned perfectly and if the satellite to receiver signal path were always unobstructed. In general, however, this is not the case; the phase data is subject to "cycle slips" or short periods of time during which the receiver loses lock on the signal. These are of concern because all carrier-phase observations are subject to ambiguity since only the fractional portion of a phase difference can be detected. (This ambiguity takes the form of an initial unknown range if integrated Doppler observations are used.) In fact, recent experience with carrier-phase data has shown that cycle slips are the major factor limiting accuracy in this type of positioning (Cannon, 1987). Therefore, the second strategy uses an inexpensive strapdown INS to bridge the gaps which occur when the receiver loses lock on the signal. In this case, all that is

15

required of the INS is that the noise level be somewhat lower than half the 19 cm wavelength of the L1 carrier, since cycle slips manifest themselves as integer numbers of wavelengths. A conceptual flowchart of the second strategy appears in Figure 2.7. The box labled "bootstrap INS" indicates the error control which is provided by GPS and which is necessary to obtain meaningful strapdown INS output.

Besides providing the functions described above, the inertial navigation systems in both strategies serve two further purposes. First, it is not practical to expect that the INS, GPS receiver, and aerial camera intervalometer (which controls the shutter) will be synchronized. Since, in gereral, the aircraft velocity will not be constant between exposures, the INS will serve to interpolate positions at the instant the shutter is open. Secondly, the GPS antenna phase centre, the reference centre of the INS, and the camera's centre of projection do not occupy the same position in space. Although the displacement vectors between these locations can be determined with respect to the aircraft structure, the orientation of these vectors will vary during the mission (Lucas, 1987). In this case, the INS can be used to monitor these changes in orientation. As will be seen in Chapter 6, however, INS data on the orientation of the camera will **not** be used as part of the photogrammetric block adjustment.
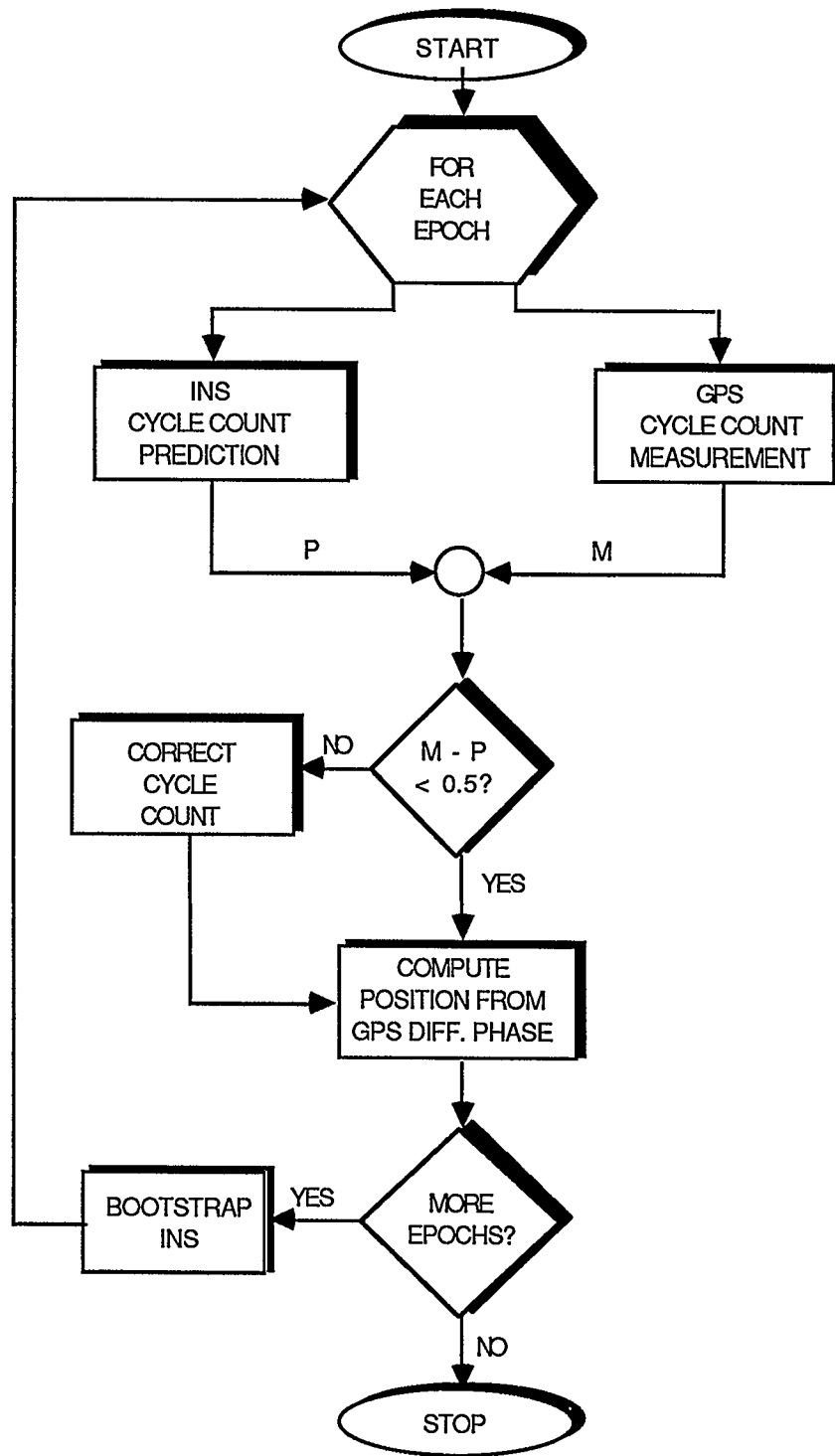
Figure 2.7. **Positioning strategy 2**

17

Chapter 3
Positioning Models

This chapter will provide a mathematical framework for processing the INS and GPS observations and will describe the error characteristics of these data. The first part of the chapter describes the various coordinate systems used. Next, the mechanization equations of inertial navigation systems are discussed, and an INS error model is presented. The local-level mechanization is emphasized; error models for strapdown INS's were not considered in this investigation. Lastly, GPS math models and error behaviour are described.

3.1 Coordinate Systems

All of the coordinate systems used in this study are right-handed Cartesian systems. Two of the coordinate systems, the *mean right ascension system* and the *orbital* system (Vanicek and Krakiwsky, 1986), are inertial in the Newtonian sense. Two of the systems are earth-referenced. Since January 1987, GPS positions have been given in the *World Geodetic System of 1984* (WGS84) (Wanless, 1987), and it will be assumed that the ellipsoid so-defined is the reference for INS positions as well (see Wong and Schwarz, 1983). The other earth-referenced frame is that maintained by the stable-platform INS used in this research; it is known as the *local level* system. The *aircraft* coordinate system is fixed with respect to the aircraft and provides a reference for the strapdown INS.

Detailed analysis requires that several other coordinate systems be defined. Some of these frames, e.g., the accelerometer and gyroscope frames, are, in general, non-orthogonal. This level of detail will not be treated here; the reader is instead referred to Britting (1971).

The coordinate systems used in aerotriangulation will be described in the second part of this thesis. The earth-referenced coordinate systems will be discussed first.

3.1.1 World Geodetic System of 1984 (WGS84)

WGS84 is a conventional terrestrial (CT) system (Vanicek and Krakiwsky, 1986) in which certain parameters of the approximate geometric figure of the earth (an ellipsoid of revolution) and of gravity have been specified. These parameters are:

angular speed of earth (ω_e)	$7.292\ 115 \cdot 10^{-5}\ \text{s}^{-1}$
ellipsoid semi-major axis (a_e)	$6\ 378\ 137.0\ \text{m}$
ellipsoid flattening (f_e)	$1 / 298.257\ 223\ 563$
gravitational constant (GM)	$3.986\ 005 \cdot 10^{14}\ \text{m}^3\ \text{s}^{-2}$
fully-normalized second degree gravity zonal harmonic	$-484.1605 \cdot 10^{-6}$

(Decker, 1986). A CT system has its origin at the centre of mass of the earth. Its z-axis is the mean spin axis of the earth, its x-axis is directed through the mean Greenwich meridian ($0°$ longitude), and its y-axis is directed so as to form a right-handed system. Figure 3.1 illustrates these axes. Coordinates in this system are designated by the superscript "CT" which preceeds them. The symbol ω_{ie}

19
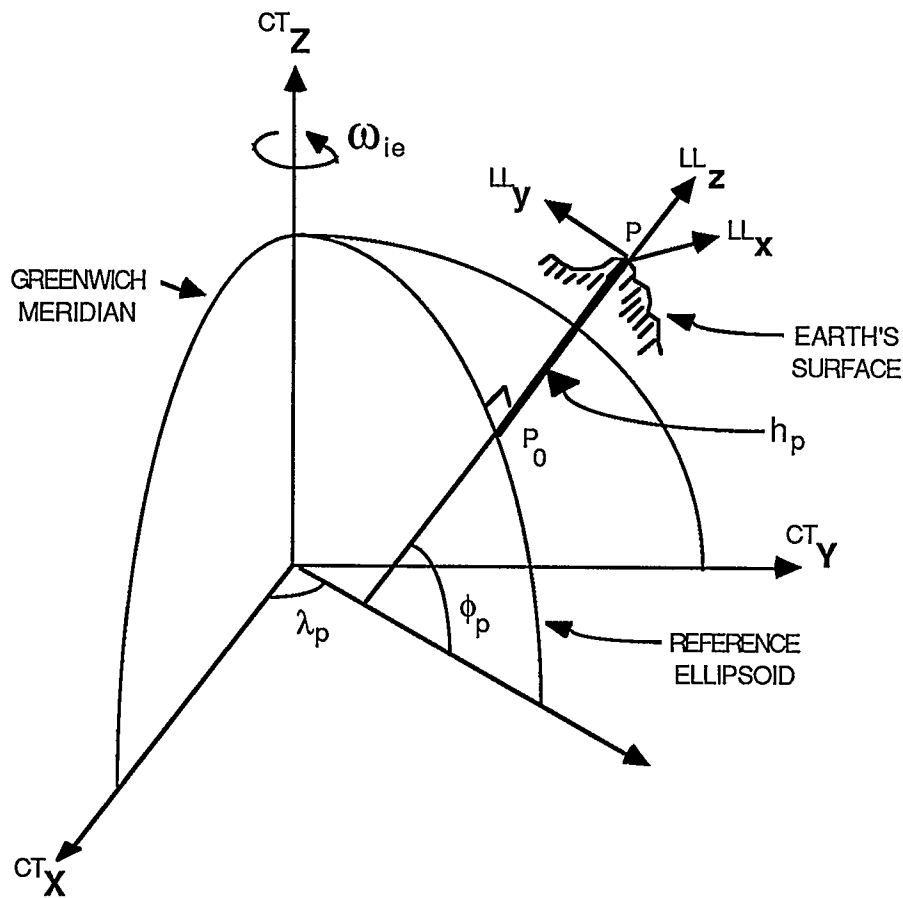
Figure 3.1. **CT and local-level coordinate systems**

designates the mean rotation vector of the earth, with the subscript "*ie*" indicating

the rotation of the earth relative to inertial space. The geodetic latitude, longitude,

and height are curvilinear coordinates in the *CT* system; these are also illustrated in

the figure. The geodetic latitude of a point P (ϕ_p) is defined as the acute angle,

measured in the ellipsopidal meridian of P, between the equatorial plane and the

ellipsoid normal through P. The longitude of P (λ_p) is the clockwise angle,

measured in the equatorial plane, between the Greenwich Meridian and the

ellipsoidal meridian of P (Vanicek and Krakiwsky, 1986). The geodetic (or

geometric) height of P (h_p) is defined as the distance along the ellipsoid normal

from the surface of the ellipsoid (at P_0 in the figure) to P. The transformations between geodetic curvilinear and Cartesian coordinates may be found in geodesy textbooks such as the one referenced above.

3.1.2 The Local Level System

The local level system has its origin in the INS. Its z-axis points up along the ellipsoidal normal, its x-axis points east, and its y-axis points north to complete the right-handed system (Wong and Schwarz, 1983). The relationship of the local level system to the CT system is illustrated in Figure 3.1. The superscript "LL" preceeding the coordinates designates them as local level. Since the particular ellipsoid to which the local level system is aligned is arbitrary; it will be assumed that the output from the stable-platform INS is available directly as WGS84 coordinate differences (ibid.).

3.1.3 The Mean Right Ascension System

This system will be the point of departure for the development of an operational inertial frame for the INS mechanization equations. Figure 3.2 illustrates the right ascension system and its relation to a CT system and to an orbital system. The xy-plane of this system is the mean celestial equator at a particular epoch T. The x-axis is directed toward the vernal equinox, denoted by the ram's head symbol in the figure, and the z-axis is the mean celestial pole at epoch T. The y-axis is directed to form a right-handed system (Mueller, 1969). The right ascension system is related to the *instantaneous terrestrial* (*IT*) system (Vanicek and Krakiwsky, 1986) by the Greenwich Apparent Siderial Time (GAST), which is defined as the angle measured counterclockwise in the equatorial plane between the

21
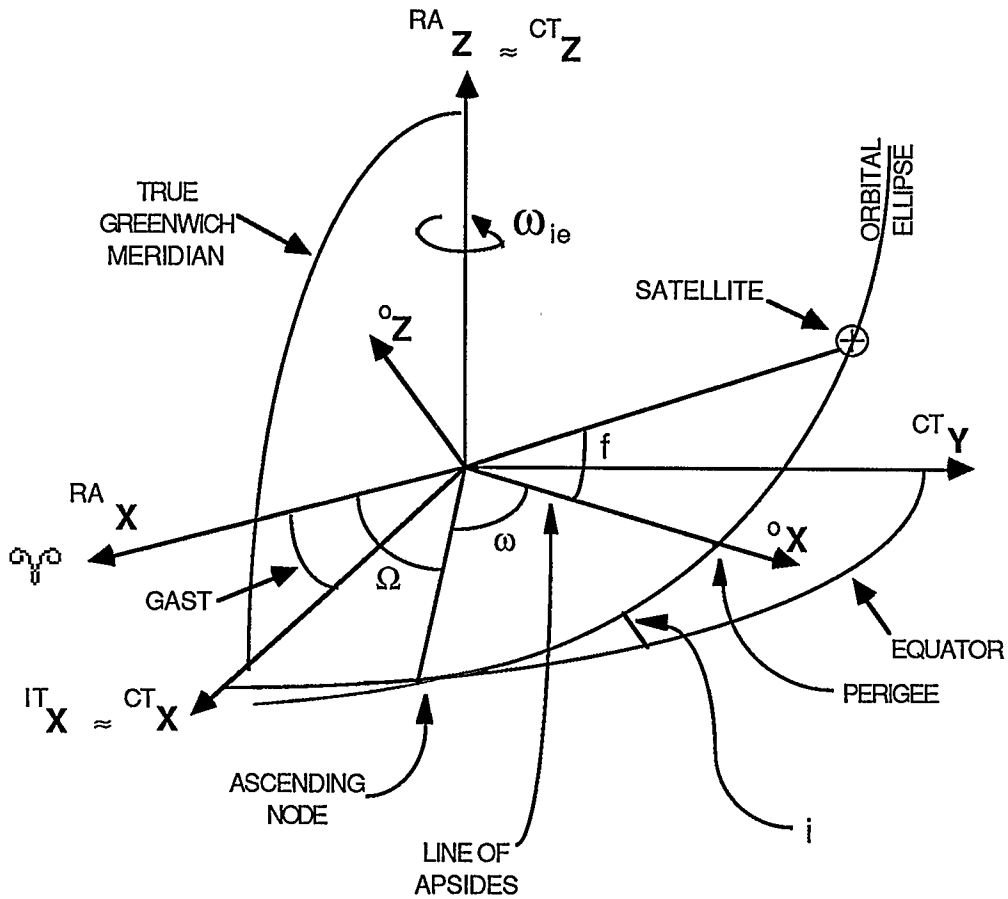
Figure 3.2. Right ascension and orbital systems

vernal equinox and the true (instantaneous) Greenwich meridian. The true Greenwich meridian differs from the mean Greenwich meridian due to polar motion, but this difference can be neglected in this study without significant consequences, as will be seen below. The approximate equality of the instantaneous and conventional terrestrial x-axes is indicated in the figure. A further simplification was made in shifting the origin of the mean right ascension system from the barycentre (the centre of mass of the solar system) to the geocentre, but, again, the consequences (due to the orbit of the earth and to gravity

field differences) are several orders of magnitude smaller than the uncertainties in INS measurements (Schwarz, 1983b). The right ascension system is denoted by the "RA" superscript.

3.1.4 Orbital Coordinate System

The orbital coordinate system, also known as the *perifocal* system (Bate et al., 1971), is a quasi-inertial system. Its origin is at the earth's centre of mass, its xy-plane contains the satellite's orbit, its x-axis is the "line of apsides" (the semi-major axis of the orbital ellipse) which connects the apogee of the orbit to the perigee, and its z-axis points in the same direction as the orbit's rotation vector. The y-axis is the semi-minor axis of the orbit, directed so as to form a right-handed system (Vanicek and Krakiwsky, 1986). The orbital system and its relation to a CT system and to the right ascension system are illustrated in Figure 3.2. The orbital system is indicated by the superscript "o" which preceeds the coordinates.

Six parameters must be defined to describe the position of the satellite in its orbit, the size of the orbit, and the position and orientation of the orbital ellipse in space. The most common representation is by the *Keplerian orbital elements* (ibid.), four of which are illustrated in Figure 3.2. These elements are:

a ... the length of the semi-major axis of the orbital ellipse (not illustrated),

e ... the eccentricity of the orbital ellipse (not illustrated),

ω ... the argument of perigee, or the angle measured counter-clockwise in the orbital plane between the ascending node (the intersection of the satellite's path northward and the equatorial plane) and the perigee,

Ω ... the right ascension of the ascending node, or the counter-clockwise angle, measured in the equatorial plane, between the vernal equinox and the ascending node,

i	... the (acute) inclination of the orbit with respect to the equatorial plane, and
f	... the true anomaly of the satellite at a particular time, or the angle between the line of apsides and the line connecting the earth's centre of mass with the satellite, measured counter-clockwise.

Cartesian orbital coordinates are obtained from the true anomaly by applying Kepler's equation, which can be found in geodesy or astrodynamics textbooks.

3.1.5 Aircraft Coordinate System

The aircraft coordinate system, denoted by the "AC" superscript, is the familiar "pitch, roll, yaw" system. This system is illustrated in Figure 3.3. In principle, the orientation of the accelerometer frame in a strapdown INS remains fixed with respect to the aircraft frame. Therefore, for convenience, it will be assumed that the aircraft and strapdown sensor frames coincide.
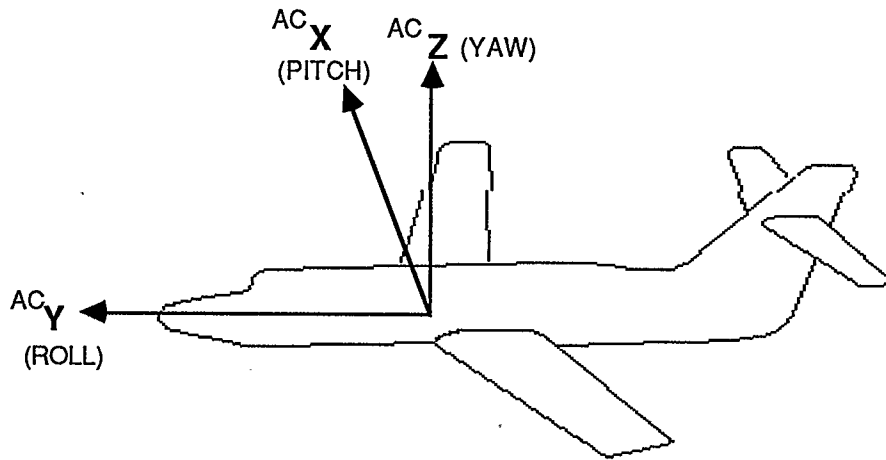
Figure 3.3.   Aircraft coordinate system

24

3.2 Models for INS Positioning

It is useful to consider first an ideal non-rotating INS moving in an inertial frame without gravitation. Positioning would then be a simple matter, since the vector of specific force measurements would be identically equal to the vector of accelerations, i.e.

$$\mathbf{f} \equiv \ddot{\mathbf{r}} \qquad (3.1)$$

where the dots indicate differentiation with respect to time. With knowledge of the initial velocity $\mathbf{v}_1$ of the INS, position differences $\Delta\mathbf{r}$ could be obtained by two successive time integrations of the specific force measurements, i.e.

$$\Delta\mathbf{r} = \mathbf{v}_1 \cdot (t_2 - t_1) + \int_{t_1}^{t_2}\int_{\tau_1}^{\tau_2} \mathbf{f} \, d\tau \, dt . \qquad (3.12)$$

In practice, the neglect of relativistic effects presents no problems because their combined magnitude is several orders smaller than the noise level of commercially-available inertial sensors (Schwarz, 1983b), but these equations must nevertheless be modified for several reasons. The first modification is due to gravity and results from the fact that gravity cannot be distinguished from other accelerations by measurement at a single point. (It is possible, however, to distinguish between gravity and other accelerations through the Riemann curvature tensor, which can be derived in part from gravity gradiometer measurements; see Moritz, 1985.) Therefore, equation (3.1) must be modified to become

25

$$\mathbf{f} = \ddot{\mathbf{r}} - \mathbf{g}^* \qquad\qquad (3.3)$$

where $\mathbf{g}^*$ is a vector of purely gravitational accelerations whose sign is arbitrary and has been chosen to conform with existing literature. Equation (3.3) has been called the *fundamental equation of inertial geodesy* (Schwarz, 1983b). It is evident that in order to extract either one of the quantities on the right of (3.3) the other quantity must be known a priori.

Secondly, in order to be useful, position differences must be related to some earth-fixed coordinate system. Lastly, noise corrupts the measurements and errors are present in the gravity reference model; these effects must be included in the equations. The formulation of INS equations in navigational coordinates and a model for error control are discussed in the next two subsections.

3.2.1 INS Mechanization Equation

The development which follows will emphasize the local-level INS mechanization, as this was the only type simulated in this study. Note that many strapdown systems are *mathematically* mechanized in the local level system.

A precise definition of an inertial reference frame is needed. As cited above, relativistic effects can be neglected without ill effect. Therefore, an inertial reference frame may be defined as one in which the Newtonian equations of motion hold (Schwarz, 1983b). A practical realization of such a system is a star catalogue system, such as the mean right ascension system (Mueller, 1969).

It is now possible to develop transformation equations between the inertial reference frame and the earth-fixed reference frames described above, and to relate

26

the INS specific force measurements to these various frames. If the proper motion of stars (Mueller, 1969) is neglected, the transformation which relates a vector $^{RA}\mathbf{r}$ in the mean right ascension system at time T_0 to a vector $^{CT}\mathbf{r}$ in the conventional terrestrial system at time T is given by

$$^{RA}\mathbf{r} \;=\; \mathbf{P^{-1}}\bullet\mathbf{N^{-1}}\bullet\mathbf{R_z}(-\text{GAST})\bullet\mathbf{R_x}(yp)\bullet\mathbf{R_y}(xp)\bullet{^{CT}}\mathbf{r} \qquad (3.4)$$

where $\mathbf{P}$ is a rotation matrix accounting for general precession from time T_0 to time T, $\mathbf{N}$ is a rotation matrix accounting for astronomic nutation from T_0 to T, $\mathbf{R_w}(\theta)$ indicates a rotation through the angle θ about the w-axis, and xp and yp are elements of polar motion from T_0 to T (ibid.). Neglected effects in this definition have magnitudes totalling $2.4 \bullet 10^{-12}$ s^{-1} in rotation and $2 \bullet 10^{-6}$ m s^{-2} in linear acceleration (Schwarz, 1983b). Measurements from commercially-available equipment have uncertainties which are much greater than this; gyroscopes have accuracies of approximately $5 \bullet 10^{-9}$ s^{-1}, and accuracies of $5 \bullet 10^{-5}$ m s^{-2} can be expected of available accelerometers. As a rule of thumb, accuracies in the reference model for an INS should be one order of magnitude better than instrumental accuracies (Schwarz, 1985a). Therefore, equation (3.4) can be simplified. This is done by approximating precession, nutation, polar motion with a mean time system which averages the effects of these phenomena (along with the earth's variable rotation rate). The relation then becomes

$$^{I}\mathbf{r} \;=\; \mathbf{R_z}(-\text{GMST}) \bullet {^{CT}}\mathbf{r} \qquad (3.5)$$

where GAST has been replaced by GMST, the Greenwich Mean Siderial Time and the superscript "RA" has been replaced by "I" to designate an operational inertial

frame (ibid.). For INS positioning, the absolute epoch is inconsequential, and GMST can be replaced by the accumulated mean time since the start of the mission. A shorthand notation, which is a variation of that found in Britting (1971), will be adapted and equation (3.5) becomes

$$^I\mathbf{r} = {}^I\mathbf{R}_{CT} \cdot {}^{CT}\mathbf{r} \tag{3.6}$$

where $^I\mathbf{R}_{CT}$ indicates a rotation from the conventional terrestrial system into the operational inertial system. The transformation from the local level system to the operational inertial system can be obtained by noting

$$^I\mathbf{R}_{LL} = {}^I\mathbf{R}_{CT} \cdot {}^{CT}\mathbf{R}_{LL} \tag{3.7}$$

where, from Figure 3.1

$$^{CT}\mathbf{R}_{LL} = \mathbf{R}_z(-90° - \lambda) \cdot \mathbf{R}_x(\phi - 90°) . \tag{3.8}$$

For the explicit elements in $^I\mathbf{R}_{CT}$, $^{CT}\mathbf{R}_{LL}$, and $^I\mathbf{R}_{LL}$, see Schwarz (1983b).

Likewise, for the aircraft coordinate system

$$^{LL}\mathbf{r}_S = {}^{LL}\mathbf{R}_{AC} \cdot {}^{AC}\mathbf{r}_S \tag{3.9a}$$

$$^{CT}\mathbf{r}_S = {}^{CT}\mathbf{R}_{AC} \cdot {}^{AC}\mathbf{r}_S \tag{3.9b}$$

$$^I\mathbf{r}_S = {}^I\mathbf{R}_{AC} \cdot {}^{AC}\mathbf{r}_S \tag{3.9c}$$

where the "s" subscripts denote the vector from the geocentre to the INS. Note that translations of vectors are freely allowed.

The alignment of the aircraft system with respect to the earth-fixed or inertial coordinate frames may change very rapidly. Therefore, various algorithms

have been developed for updating the transformation matrices quickly in strapdown INS's. A commonly-used algorithm expands the rotation matrices in terms of unit quaternions, in which algebraic combinations of four parameters replace the trigonometric functions in the matrices (VanBronkhorst, 1978).

Relations may now be obtained between velocities and accelerations in the various frames by differentiating equations of the form of (3.6) or (3.9) with respect to time. For the case of the local level to operational inertial frame transformation, the first derivative is

$$\dot{^I\mathbf{r}} = \dot{^I\mathbf{R}_{LL}} \cdot {^{LL}\mathbf{r}} + {^I\mathbf{R}_{LL}} \cdot \dot{^{LL}\mathbf{r}} . \tag{3.10}$$

From Britting (1971), the time derivative of an orthogonal rotation matrix is given by

$$\dot{^j\mathbf{R}_i} = {^j\mathbf{R}_i} \cdot {^i\Omega_{ji}} \tag{3.11}$$

where ${^i\Omega_{ji}}$ is a skew-symmetric matrix composed of the elements of the rotation vector of the i system relative to the j system coordinatized in the i system; specifically

$$^i\Omega_{ji} = \begin{bmatrix} 0 & -\omega_z & \omega_y \\ \omega_z & 0 & -\omega_x \\ -\omega_y & \omega_x & 0 \end{bmatrix} \tag{3.12a}$$

where ω_x, ω_y, and ω_z are the components of the rotation vector. Note that

$$^i\Omega_{ji} = -\,^i\Omega_{ij}\,.\tag{3.12b}$$

Equation (3.10) may then be rewritten as

$$^I\dot{\mathbf{r}} = \,^I\mathbf{R}_{LL}\cdot(^{LL}\Omega_{ILL}\cdot\,^{LL}\mathbf{r} + \,^{LL}\dot{\mathbf{r}})\tag{3.13}$$

which is the Coriolis law in matrix notation (ibid.).

For the remainder of this development, it will be assumed that both the stable-platform and strapdown INS's are mechanized in the local level frame. In the former case the mechanization is by hardware; in the latter it is accomplished with software. Note that

$$^{LL}\mathbf{f} = \,^{LL}\mathbf{R}_{AC}\cdot\,^{AC}\mathbf{f}\,.\tag{3.14}$$

A similar transformation is needed to convert gyroscope rate measurements in the aircraft system to rates in the local level system. For details on these transformations, see VanBronkhorst (1978).

As mentioned in §2.1, the INS mechanization is usually done in terms of a velocity, which is defined as

$$\overset{LL}{} \mathbf{v} \equiv \overset{LL}{} \mathbf{R}_{CT} \cdot \overset{CT}{} \dot{\mathbf{r}}_S \qquad (3.15)$$

(Britting, 1971). After differentiation and algebraic manipulation, the following expression is obtained

$$\overset{LL}{} \dot{\mathbf{v}} = \overset{LL}{} \mathbf{R}_I \cdot \overset{I}{} \ddot{\mathbf{r}} - (\overset{LL}{} \Omega_{CTLL} + 2 \overset{LL}{} \Omega_{ICT}) \cdot \overset{LL}{} \mathbf{v}$$

$$- \overset{LL}{} \Omega_{ICT} \cdot \overset{LL}{} \Omega_{ICT} \cdot \overset{LL}{} \mathbf{r}_S. \qquad (3.16)$$

The last two terms on the right side of equation (3.16) are the Coriolis and centripetal accelerations, respectively. This equation is derived in the appendix.

A relationship between $\overset{LL}{} \mathbf{f}$, the specific force vector in the local level system, and the geographic positions, velocities, and velocity rates can now be developed. First, equation (3.3) is transformed to

$$\overset{LL}{} \mathbf{f} = \overset{LL}{} \mathbf{R}_I \cdot \overset{I}{} \ddot{\mathbf{r}} - \overset{LL}{} \mathbf{g}^*(\mathbf{r}_S) \qquad (3.17)$$

where the argument $\mathbf{r}_S$ has been added to $\overset{LL}{} \mathbf{g}^*$ to indicate the dependence of gravitation on position. Note that lunisolar and planetary tides, having a combined magnitude of approximately $2 \cdot 10^{-7}$ times gravity, have been neglected (Schwarz, 1983b). The gravitational vector $\overset{LL}{} \mathbf{g}^*$ can be replaced by the gravity vector

$$\overset{LL}{} \mathbf{g}(\mathbf{r}_S) = \overset{LL}{} \mathbf{g}^*(\mathbf{r}_S) - \overset{LL}{} \Omega_{ICT} \cdot \overset{LL}{} \Omega_{ICT} \cdot \overset{LL}{} \mathbf{r}_S \qquad (3.18)$$

which includes the centripetal acceleration. Using equation (3.18) in (3.17), and combining the result with equation (3.16), the mechanization equation in the local level system results, which is

$$^{LL}\dot{\mathbf{v}} = {}^{LL}\mathbf{f} - ({}^{LL}\Omega_{CTLL} + 2{}^{LL}\Omega_{ICT}) \bullet {}^{LL}\mathbf{v} + {}^{LL}\mathbf{g}(\mathbf{r}_s) . \qquad (3.19)$$

3.2.2 Local-Level INS Error Model

The direct application of equation (3.19) would require perfect sensors and perfect knowledge of the earth's gravity field. Since neither of these conditions can be met, sensor and gravity model imperfections must be incorporated. In order to solve (3.19) and to take advantage of well-known estimation techniques, a linear error model is desired. The system of differential equations (3.19), however, is nonlinear, since $^{LL}\mathbf{v}$ is implicit in $^{LL}\Omega_{CTLL}$. The linearization of the error equations is accomplished by using perturbation techniques (Britting, 1971). Using these techniques, the system errors and gravity model imperfections are expressed as linear perturbations about an approximate reference trajectory and gravity reference model. Thus, the following substitutions are made:

$$^{LL}\dot{\mathbf{v}} = {}^{LL}\dot{\mathbf{v}}_0 + \delta\dot{\mathbf{v}} \qquad (3.20a)$$

$$^{LL}\mathbf{g} = \gamma + \delta\mathbf{g} \qquad (3.20b)$$

The reference trajectory is given by

$$^{LL}\dot{\mathbf{v}}_0 = {}^{LL}\mathbf{f} - ({}^{LL}\Omega_{CTLL} + 2{}^{LL}\Omega_{ICT})_0 \bullet {}^{LL}\mathbf{v}_0 + \gamma \qquad (3.20c)$$

where the "0" subscripts denote approximation and the vector γ is a standard gravity model known as *normal gravity*, which is the gravity of a fictitious equipotential ellipsoid which has the same total mass as the earth (Heiskanen and Moritz, 1967). Formulae for the computation of normal gravity (which is a function of latitude and height), as well as the definition of the components of the gravity disturbance vector δg can be found in the cited reference. In principle, the known portion of the gravity disturbance vector can be included in the reference model, but this is usually not done.

Time-dependent errors in local level INS's account for about 95% of the total error (Goldfarb and Schwarz, 1985), and these errors will be emphasized The time-dependent portion of the error model is of the form

$$\ddot{\delta v} = \ddot{\delta v}(\delta \varepsilon, \delta b, \delta g'; t, f, w) \qquad (3.21)$$

where

$\delta \varepsilon$ is a set of initial sensor errors which propagate in a well-defined fashion

δb is a set of nonlinear sensor errors

$\delta g'$ is the unmodeled portion of the gravity disturbance vector

f is the specific force vector, and

w is a vector of random forcing functions

(Schwarz, 1985b).

If the reference trajectory is sufficiently close to the true trajectory, equation (3.21) can be expressed in *state-space* notation (Gelb, 1974) as

$$\dot{\mathbf{x}}(t) = \mathbf{F}(t) \cdot \mathbf{x}(t) + \mathbf{w}(t) \qquad (3.22a)$$

with initial conditions

$$\mathbf{x}(0) = \mathbf{x}_0 . \qquad (3.22b)$$

The vector $\mathbf{x}(t)$ is known as the *state vector*; in this case it is composed of error states. $\mathbf{F}(t)$ is known as the *dynamics matrix*, and its nature depends on the particular error states chosen. There are an infinity of choices for the components of the state vector, and a rigorous INS error model would require many scores of error states. In practice, individual error states are lumped to make the formulation and computations tractable. A common formulation uses twelve error states: six to specify translation and translation rates, and six to specify orientation and orientation rates (Schwarz, 1985b).

In order to obtain a solution to equation (3.22), $\mathbf{F}(t)$ is assumed to be time invariant. In practice, this is done by choosing time intervals for the solution which are sufficiently short to make this assumption valid. The solution to the nonhomogeneous equation (3.22) is then given by

$$\mathbf{x}(t) = \Phi(t,t_0) \cdot \mathbf{x}_0 + \int_{t_0}^{t} \Phi(t,\tau) \cdot \mathbf{w}(\tau) \, d\tau . \qquad (3.23)$$

$\Phi(t, t_0)$ is known as the *state transition matrix* from time t_0 to time t and is given by the matrix exponential

$$\Phi(t,t_0) = e^{\mathbf{F}(t-t_0)} \qquad (3.24)$$

34

(Gelb, 1974). If the number of error states is relatively small, an analytical solution for the transition matrix can be obtained, for example, by using Laplace transform techniques (Wong, 1982). Otherwise, numerical techniques can be used, such as replacing (3.24) with the first few terms of its Taylor series. For a local-level INS, the transition matrix is dominated by trigonometric terms in the earth rate ω_{ie} and the Schuler rate ω_s, given by

$$\omega_s = \left(\frac{g}{r_s}\right)^{\frac{1}{2}} \tag{3.25}$$

where $g = |\mathbf{g}|$ and $r_s = |\mathbf{r}_s|$ (but is usually approximated by the mean earth radius). It is interesting to note that the Schuler rate is the frequency of a hypothetical point-mass pendulum whose length is $\mathbf{r}_s$.

Most INS applications require real-time positions. Furthermore, in order to assure that the error behaviour remains linear, a reasonable reference trajectory must be used and real-time state variable estimation is needed. Consequently, sequential techniques such as Kalman filtering (Gelb, 1974) are most commonly used for state vector estimation. As mentioned in §2.1, the most common form of external observations for surveying applications is the ZUPT. For positioning strategy two, a Kalman filter with GPS range-rate (Doppler) updates can be used to bootstrap the strapdown INS.

For positioning strategy one, real-time positons are not needed (except for maintainance of the reference trajectory). Therefore, a batch procedure, known as *spectral decomposition* (Schwarz, 1983a; Vassiliou, 1984) has been applied to the "raw" INS data post-mission. The use of the spectral decomposition model simplified the INS simulation considerably. The predominance of sinusoids in the

earth and Schuler frequencies in the transistion matrix forms the basis for this method. In this method, the terms in the discrete version of the error equation (3.23) are reordered and are expressed in the form

$$\delta \mathbf{r}_i = \mathbf{A}_i \cdot \mathbf{y} + \varepsilon \qquad (3.26)$$

where

$\delta \mathbf{r}_i$ is a vector of position errors at time t_i,

$\mathbf{A}_i$ is a matrix composed of base functions in the earth and Schuler frequencies which are evaluated at time t_i,

$\mathbf{y}$ is a set of coefficients which are linear combinations of the initial state errors $\mathbf{x}_0$, and

ε is a noise vector .

Specifically, the elements of the vector $\delta \mathbf{r}_i$ are

$$\delta\lambda(t_i) = a_0 + a_1 \cdot t_i + a_2 \cdot \sin(\omega_{ie} \cdot t_i) + a_3 \cdot \cos(\omega_{ie} \cdot t_i) + a_4 \cdot \sin(\omega_s \cdot t_i)$$

$$+ \; a_5 \cdot \cos(\omega_s \cdot t_i) + a_6 \cdot t_i \cdot \sin(\omega_s \cdot t_i) + a_7 \cdot t_i \cdot \cos(\omega_s \cdot t_i) + \varepsilon_\lambda \qquad (3.27a)$$

$$\delta\phi(t_i) = b_0 + b_1 \cdot t_i + b_2 \cdot \sin(\omega_{ie} \cdot t_i) + b_3 \cdot \cos(\omega_{ie} \cdot t_i) + b_4 \cdot \sin(\omega_s \cdot t_i)$$

$$+ \; b_5 \cdot \cos(\omega_s \cdot t_i) + b_6 \cdot t_i \cdot \sin(\omega_s \cdot t_i) + b_7 \cdot t_i \cdot \cos(\omega_s \cdot t_i) + \varepsilon_\phi \qquad (3.27b)$$

$$\delta h(t_i) = c_0 + c_1 \cdot \sinh(\kappa \cdot t_i) + c_2 \cdot \cosh(\kappa \cdot t_i) + c_3 \cdot \sin(\omega_{ie} \cdot t_i)$$

$$+ \; c_4 \cdot \sin(\omega_s \cdot t_i) + c_5 \cdot \cos(\omega_s \cdot t_i) + c_6 \cdot t_i \cdot \cos(\omega_s \cdot t_i) + \varepsilon_h \qquad (3.27c)$$

where $\delta\lambda$, $\delta\phi$, and δh are errors in longitude, latitude, and height, respectively, and κ is a damping factor. For the relationship of these quantities to the initial state vector and the transition matrix, see Vassiliou (1984). The vector $\mathbf{y}$ and matrix $\mathbf{A}_i$ are given by

$$\mathbf{y} \;=\; \begin{bmatrix} \mathbf{a} \\ \mathbf{b} \\ \mathbf{c} \end{bmatrix} \tag{3.28a}$$

$$\mathbf{A}_i \;=\; \begin{bmatrix} \mathbf{A}^*_1 & 0 & 0 \\ 0 & \mathbf{A}^*_1 & 0 \\ 0 & 0 & \mathbf{A}^*_2 \end{bmatrix} \tag{3.28b}$$

where

$$\mathbf{a} \;=\; [a_0, a_1, a_2, a_3, a_4, a_5, a_6, a_7]^T \tag{3.29a}$$

$$\mathbf{A}_1^* \;=\; [1, t_i, \sin(\omega_{ie} \cdot t_i), \cos(\omega_{ie} \cdot t_i), \sin(\omega_s \cdot t_i), \cos(\omega_s \cdot t_i), t_i \cdot \sin(\omega_s \cdot t_i),$$
$$t_i \cdot \cos(\omega_s \cdot t_i)] \tag{3.29b}$$

and $\mathbf{b}$, $\mathbf{c}$, and $\mathbf{A}_2^*$ are formed in an analogous manner.

There are a number of other errors which are not time-dependent but instead are roughly proportional to the magnitude of the coordinate differences obtained during the mission. Major errors of this type are due to accelerometer scale factor uncertainties and to nonorthoganalities of the accelerometer frame.

These errors can be added to equations (3.28) by augmenting **y** and **A**$_i$ (Goldfarb and Schwarz, 1985). However, since these errors account for less than five percent of the total error, they have not been included in this study.

For positioning strategy one, estimation of the vector δr is accomplished by fitting equations (3.28) to the discrepancies between the raw INS positions and the positions derived from GPS differential P-code pseudoranges. The processing of INS and GPS data is discussed in Chapter 4.

3.3 Models for GPS Positioning

GPS was designed to provide instantaneous position and time by ranging to four satellites simultaneously. Each measured pseudorange can be represented by

$$_s\rho_i = [(x_s-x_i)^2 + (y_s-y_i)^2 + (z_s-z_i)^2]^{1/2} + c'\delta t_i - c'\delta t_s + \delta_{ion} + \delta_{trop} + _s\varepsilon_i$$

$$(3.30)$$

where

$_s\rho_i$	...is the pseudorange from receiver i to satellite s,
x_s, y_s, z_s	...are the Cartesian coordinates of satellite s,
x_i, y_i, z_i	...are the Cartesian coordinates of receiver i,
c'	...is the average propagation speed of the signal from s to i,
δt_i	...is the instantaneous receiver clock bias (to be estimated),
δt_s	...is the portion of the satellite clock error computed from the navigation message,
δ_{ion}	...is the computed range-equivalent ionospheric group delay,
δ_{trop}	...is the computed range-equivalent tropospheric delay, and

38

$$_s\varepsilon_i \qquad \text{...is the sum of all undetermined effects in } _s\rho_i.$$

As mentioned in §2.2, differential pseudoranges were used in this research. A pseudorange difference can be expressed as

$$\Delta_s\rho_{12} = \frac{_s\mathbf{e}_1 + _s\mathbf{e}_2}{1 + _s\mathbf{e}_1 \cdot _s\mathbf{e}_2} \cdot \Delta\mathbf{r}_{12} + c'\Delta\delta t_{12} + c'\Delta\delta_{ion} + c'\Delta\delta_{trop} + \Delta_s\varepsilon_{12} \qquad (3.31)$$

where

$\Delta_s\rho_{12}$	$= {_s\rho_1} - {_s\rho_2},$	
$\Delta\delta t_{12}$	$= \delta t_1 - \delta t_2,$	
$_s\mathbf{e}_1, _s\mathbf{e}_2$	...are unit vectors pointing from the receivers to satellite s,	
$\mathbf{r}_1, \mathbf{r}_2$	...are the geocentric position vectors of the receivers,	
$\Delta\mathbf{r}_{12}$	...is the baseline vector from receiver 1 to receiver 2,	
$\Delta\delta_{ion}$	...is the difference between the ionospheric corrections applied to the individual ranges,	
$\Delta\delta_{trop}$	...is the difference between the tropospheric corrections applied to the individual ranges,	
$\Delta_s\varepsilon_{12}$	...is the difference in unmodeled effects between the pseudoranges,	

and the indicated products are scalar products (Vanicek et al., 1984). Range and range difference geometry is shown in Figure 3.4. Note that equation (3.31) is linear in the components of $\Delta\mathbf{r}_{12}$, and its solution can be obtained by successive substitution of the components of $_s\mathbf{e}_1$, $_s\mathbf{e}_2$, $\mathbf{r}_1$ and $\mathbf{r}_2$.
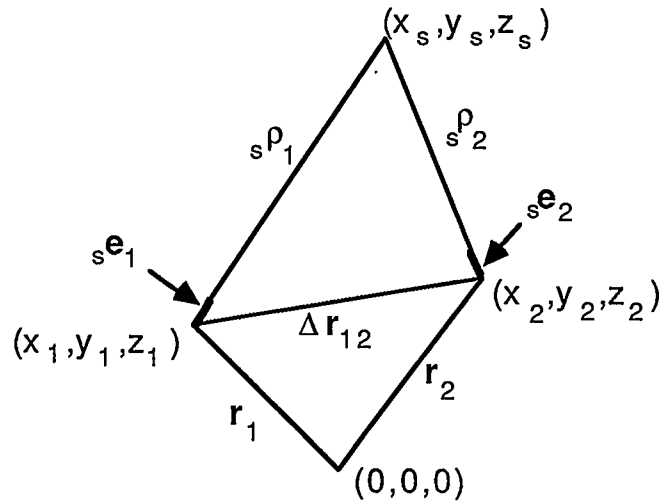
Figure 3.4.   Range and range difference geometry

There are several different models for GPS phase observations which involve differencing between receivers, between epochs, or between satellites (Remondi, 1984; Cannon, 1987). The model chosen for use here is the single difference, which is obtained by scaling equation (3.31) by the wavelength of the carrier and by adding a term representing an integer ambiguity. A single-difference phase measurement can be expressed (in simplified form) as

$$\Delta_s\phi_{12} = \frac{f}{c} \cdot \left[\frac{{}_s e_1 + {}_s e_2}{1 + {}_s e_1 \cdot {}_s e_2} \cdot \Delta r_{12} + c'\Delta\delta t_{12} + \Delta\delta_{ion} + \Delta\delta_{trop} \right] + \Delta_s\varepsilon_{\phi 12} + {}_s N_{12}$$

(3.32)

where

$\Delta_s\phi_{12}$ ...is the difference between the instantaneous
            phase measurements at receivers 1 and 2,

f ...is the carrier frequency (in Hertz),

c ...is the speed of light in vacuum,

40

$\Delta_s\varepsilon_{\phi12}$ ...represents unmodeled effects in $\Delta_s\phi_{12}$, and

$_sN_{12}$ ...is the integer difference in the number of wavelengths in the rays from satellite s to the receivers (plus an arbitrary integer bias).

For a more detailed model, see Remondi (1984).

In order for this equation to be useful, all ambiguities $_iN_{12}$ must be determined. This is easily done by placing the receivers on a fixed baseline and treating the ambiguities as unknown parameters to be estimated along with the baseline components. The ambiguities can usually be resolved with less than one-half hour of observations if the baseline components are unknown (Wanless, 1987). Less time is required if there is good a priori knowledge of the baseline components. Another technique for ambiguity resolution, which uses an adaptive Kalman filter, may also be applicable to kinematic positioning (Brown and Hwang, 1984). For an aerial photography mission, the integers could be determined from data collected before the plane takes off. Once the ambiguity is resolved, the accumulated cycle count is tracked at each receiver. However, if one of the receivers loses lock on a satellite's signal, or if a new satellite is selected, a new ambiguity parameter must be determined. In either case, the output of an inexpensive strapdown INS could be used to aid the process.

3.3.1 GPS Error Model

The major error sources categorized in §2.2 are repeated here:

1. Satellite
    - orbit prediction errors
    - satellitie clock errors

2. Propagation
    - ionospheric group delay uncertainties
    - unmodeled tropospheric delay

3. Receiver
    - multipath effects
    - receiver noise and truncation error .

The errors induced by these sources in ranges, range differences, and phase differences propagate into the coordinates or coordinate differences which are being estimated. The magnitudes of the errors in the estimated parameters are functions of the satellite-receiver geometry. The error sources and geometrical considerations will be discussed in turn.

1. Satellite uncertainties

Orbit prediction errors arise for several reasons. Firstly, for expediency, a simplified ephemeris representation is broadcast. Secondly, satellite perturbations are not completely predictable because there is incomplete knowledge of perturbing forces, especially solar radiation pressure. Finally, the relative positions of the tracking stations are not known exactly, and errors in tracking station coordinates and tracking measurements propagate into the orbit.

GPS was designed for single receiver operation using pseudoranges. Consequently, the allowable spatial distribution of orbit uncertainties in the broadcast ephemeris is based on the contribution of these errors to the "user range error" (URE). Divine and Francisco (1984) used the following formula to express the relationships of the orbit and satellite clock errors in the error budget:

$$\text{URE} = \left(\varepsilon_R^2 + \frac{\varepsilon_T^2}{50} + \frac{\varepsilon_N^2}{50} + c^2 \varepsilon_t^2 - 2 \Psi_{Rt} \cdot \varepsilon_R \cdot \varepsilon_t \right)^{\frac{1}{2}} \qquad (3.33)$$

where

ε_R ...is the radial orbit uncertainty,

ε_T ...is the tangential orbit uncertainty,

ε_N ...is the cross-track orbit uncertainty,

c ...is the speed of light,

ε_t ...is the satellite clock uncertainty, and

Ψ_{Rt} ...is the cross-correlation between ε_R and ε_t.

As would be expected for single-receiver pseudoranging, tangential and cross-track orbit errors are allowed to be quite a bit larger than radial orbit or satellite clock errors. With a projected URE of six metres, tangential and cross-track uncertainties in broadcast ephemeris can reach 25 metres or more (Swift, 1985).

A property of the broadcast ephemeris which has significance in this study is its smoothness. Smoothness in the ephemeris implies that uncertainties in satellite positions will manifest themselves as slowly-changing biases. For the observation time span used in this study (84 minutes), these uncertainties are treated as random constants.

The parameters in the broadcast ephemeris are changed every hour. Therefore, an indication of the internal consistency of the data can be obtained by computing the satellite coordinates at the division point between ephemeris blocks using the coefficients in each block (i.e. forward and backward) and examining the resulting coordinate differences. For this purpose, broadcast ephemeris data

43

spanning four days in January, 1985 were reduced using the algorithm outlined in Van Dierendonck et al. (1980). The resulting differences, expressed in conventional terrestrial coordinates, are summarized in Table 3.1. Note that in all cases the discrepancies are one or more orders of magnitude smaller than the expected uncertainties.

	CT_X	CT_Y	CT_Z
rms	0.08	0.12	0.09
maximum	3.08	4.23	3.48

Table 3.1.   Ephemeris discrepancies (m)

Ironically, for range differences, radial orbit errors are more easily tolerated than tangential and cross-track uncertainties. Nevertheless, the effects of all orbit errors on differential positions are negligible unless very high precision (e.g. one part in 10⁻⁷) is needed (Beser and Parkinson, 1984; Krakiwsky et al., 1985). This conclusion is supported by the simulation results presented in Chapter 4 of this thesis. Satellite clock errors are effectively eliminated by differencing between receivers.

2.Propagation uncertainties

The group delay induced by the ionosphere on a radio signal is a function of the frequency of the signal and the integrated electron count along the ray path. The most effective way to minimize ionospheric uncertainties is to take advantage of

the frequency dependence of the ionospheric delay by using a two-frequency receiver. In this study, however, a single-frequency receiver has been assumed. In this case a good deal of uncertainty can be removed by using differential pseudoranges. Remaining uncertainties are then due to the difference in the elevation angles at the receivers (resulting in different signal path lengths through the ionosphere), and, less significantly, to random scintillations along the independent ray paths (Denaro, 1984). The worst-case ionosphere-induced error in differential ranges for a 50 kilometre receiver separation should not exceed 1.1 metres (Kalfus et al., 1984). For the simulations in this study, an empirical formula for ionospheric delay as a function of elevation angle was used; see Chapter 4 for details.

Tropospheric delays are usually estimated by using surface meteorological measurements. Surface measurements are effective for estimating the dry component of tropospheric delay, but are less effective for estimating the wet component (Fell, 1980). The dry component, however, accounts for 80-90% of the total delay (Spilker, 1980). Uncertainties can grow quite large at low elevation angles. For this reason, observations below 5° are not used.

The troposphere above 12 000 metres contributes very little to the wet component of the delay. Therefore, because this study concerns an aircraft flying at a moderately high altitude (7 600 metres), there will be little correlation between the tropospheric uncertainties at the aircraft and at the ground, and little reduction in these effects is obtained by using the differential technique.

For the tropospheric model used in this research, see Chapter 4.

3. Receiver effects

Multipath errors arise when a portion of the received signal is reflected off nearby objects. These effects are a function of the antenna's directionality and

surroundings. Multipath errors can be minimized by antenna design, judicious placement of the antenna, and by using digital filtering techniques (Bletzacker, 1985). In this study, the receivers used for differential ranging are at least 75 kilometres apart. Therefore, the multipath errors will be independent and are not reduced by range differencing.

Receiver noise and resolution are functions of the receiver's design and operating environment and of the type of measurement used. Both noise and truncation effects are reduced by at least an order of magnitude if code measurements are replaced by phase measurements (Martin, 1980).

Geometrical considerations

The magnitude of errors in coordinates or coordinate differences resulting from errors in ranges or range differences can be approximated by a covariance analysis. Specifically, the a posteriori covariance of the estimated quantities is given by the transformation

$$C_{\langle x \rangle} = (A^T \cdot C_l^{-1} \cdot A)^{-1} \qquad (3.34)$$

where

$C_{\langle x \rangle}$ ...is the covariance matrix ot the estimated coordinates (or coordinate differences) and clock bias,

A ...is the Jacobian or *design* matrix composed of the partial derivatives of the observations with respect to the to the estimated parameters,

C_l ...is the covariance matrix of the range or range difference observations,

and the brackets $\langle \rangle$ denote estimation (Mikhail, 1976). The matrix A is strictly a function of the satellite-receiver geometry, and an estimate of the geometrical contribution to parameter uncertainties can be obtained by replacing C_l with the

46

identity matrix in equation (3.34). In navigation, the square root of the trace of the resulting parameter covariance matrix, known as the *dilution of precision* (DOP), is often used to select a particular observation geometry. Most GPS receivers are only capable of tracking four satellites. In this case, the minimization of DOP factors can be used as the criterion for selecting the best combination of satellites from all visible satellites. For GPS single-receiver operation, the diagonal elements of **A** can be obtained from equation (3.30) and are of the form

$$a_{11}, a_{22}, a_{33} = \frac{x_i - x_s}{r_{is}}, \text{ etc.} \tag{3.35a}$$

$$a_{44} = 1 \tag{3.35b}$$

where r_{is} is the geometric range from receiver i to satellite s and the range-equivalent time bias $c'\delta t_i$ is the fourth parameter being estimated. Note that a_{11}, a_{22}, and a_{33} are the elements of the unit vector from the satellite to receiver i. It can be demonstrated that the trace of the covariance matrix $C_{\langle x \rangle}$ is minimized by maximizing the volume of the tetrahedron having vertices at the four satellites. This is accomplished by selecting one satellite near the zenith and selecting three others widely distributed around the observation horizon.

If the distance between the receivers is small compared with the range to each satellite (as it was in this study), $_se_1 \approx {}_se_2$ in equation (3.31) and, therefore, the DOP factors for differential positioning can be approximated by the corresponding factors for single receiver ranging.

Note that for static positioning the instantaneous DOP factors are less significant than the integrated DOP factors over the observation period (Wanless, 1987).

Chapter 4

Positioning Simulation, Processing, and Results

A simulation package has been written in order to test the aircraft positioning strategies outlined in Chapter 2. This chapter describes this package, discusses the processing of the simulated GPS and INS observations, and presents simulation results.

4.1 Simulation

The structure of the simulation program "fltsim" is illustrated in Figures 4.1a and 4.1b. Each ot the elements of this program are discussed below.

4.1.1 Simulation Input

The major input parameters specify the location and size of the flight pattern, the locations of ground receivers for differential GPS ranges, the altitude and speed of the aircraft, the approximate GPS update interval, the condition of the atmosphere at the aircraft and on the ground, and the size and nature of the random and systematic errors applied to the INS and GPS data. Other input parameters are provided for the photogrammetric simulation, and some of these are used to determine the flight configuration.
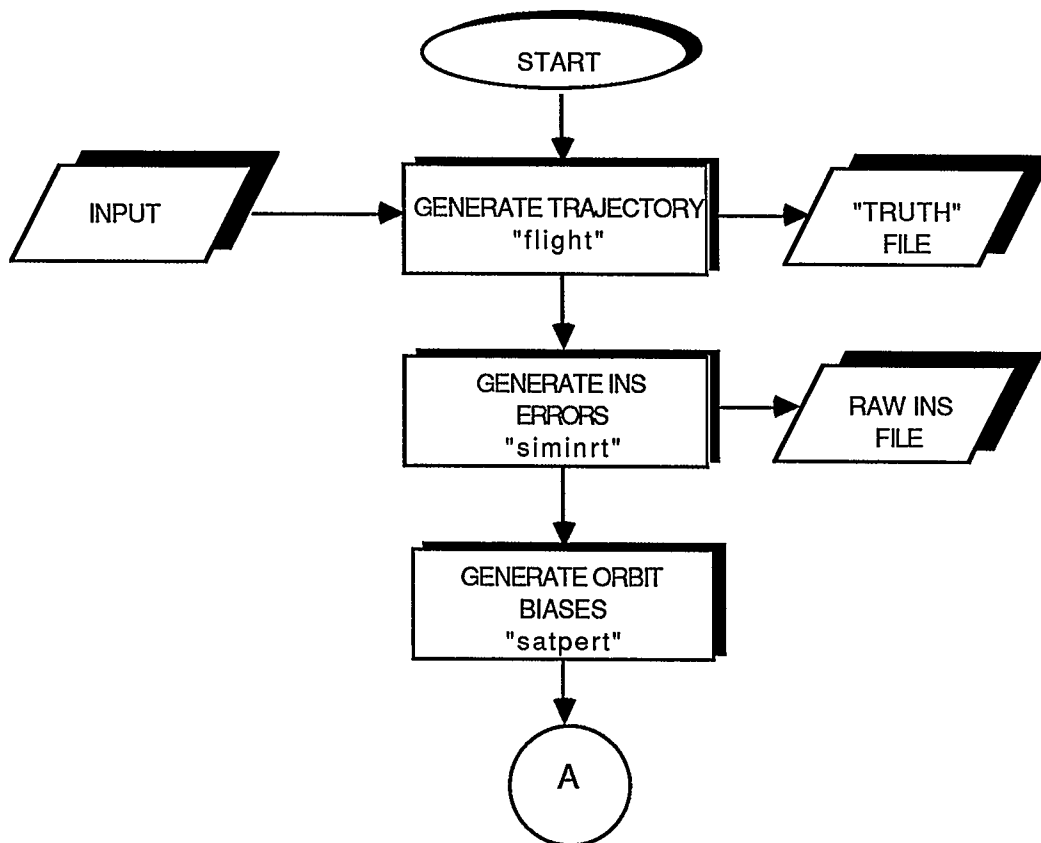
Figure 4.1a.   Simulation program "fltsim"

4.1.2 Trajectory Generation

Subroutine "flight" generates a trajectory for a photogrammetric mission. For convenience, all flight lines are laid out east or west. The spacing between exposures and flight lines is determined using the flight altitude, the camera focal length, and the percentage of overlap in adjacent photos. The GPS update interval is determined in this routine as a multiple or sub-multiple of the computed exposure interval. During the processing a binary "truth file" is written for later comparison with the positions derived from the simulated INS and GPS observations.

49

4.1.3 INS Simulation

Subroutine "siminrt" is used to simulate INS data for the mission. INS postitions are computed at each update or exposure epoch, whichever occurs more often. Equations (3.27) are used to compute perturbations to the true positions. The stochastic coefficients **a, b,** and **c** are generated with standard deviations supplied by the user. The noise terms ε can be generated as first-order Markov processes or as random walks (Gelb, 1974), at the user's discretion. The perturbed INS postions are written to a file for later analysis.

4.1.4 Orbit Perturbations

As was discussed in Chapter 3, orbit errors can be treated as constant biases for the relatively short observation periods considered in this study. Therefore, perturbations can be conveniently computed for each orbit before the actual satellite positions are generated. GPS orbits are nearly circular; eccentricities are less than 0.01 in all cases (Buffett, 1985). Consequently, circular orbits are simulated, and two of the Keplerian elements - the eccentricity and the argument of the perigee - are superfluous. Subroutine "satpert" generates random biases in three of the remaining orbital elements: the semi-major axis (radius), the inclination (cross-track), and the satellite anomaly (along-track). These biases are generated separately for each of the 18 satellites in the operational constellation. Standard deviations of these elements are supplied by the user.

4.1.5 Satellite Position Computation

Subroutine "satpos" computes positions of all satellites in the constellation at each update epoch using the perturbed orbital elements discussed above. The 18-
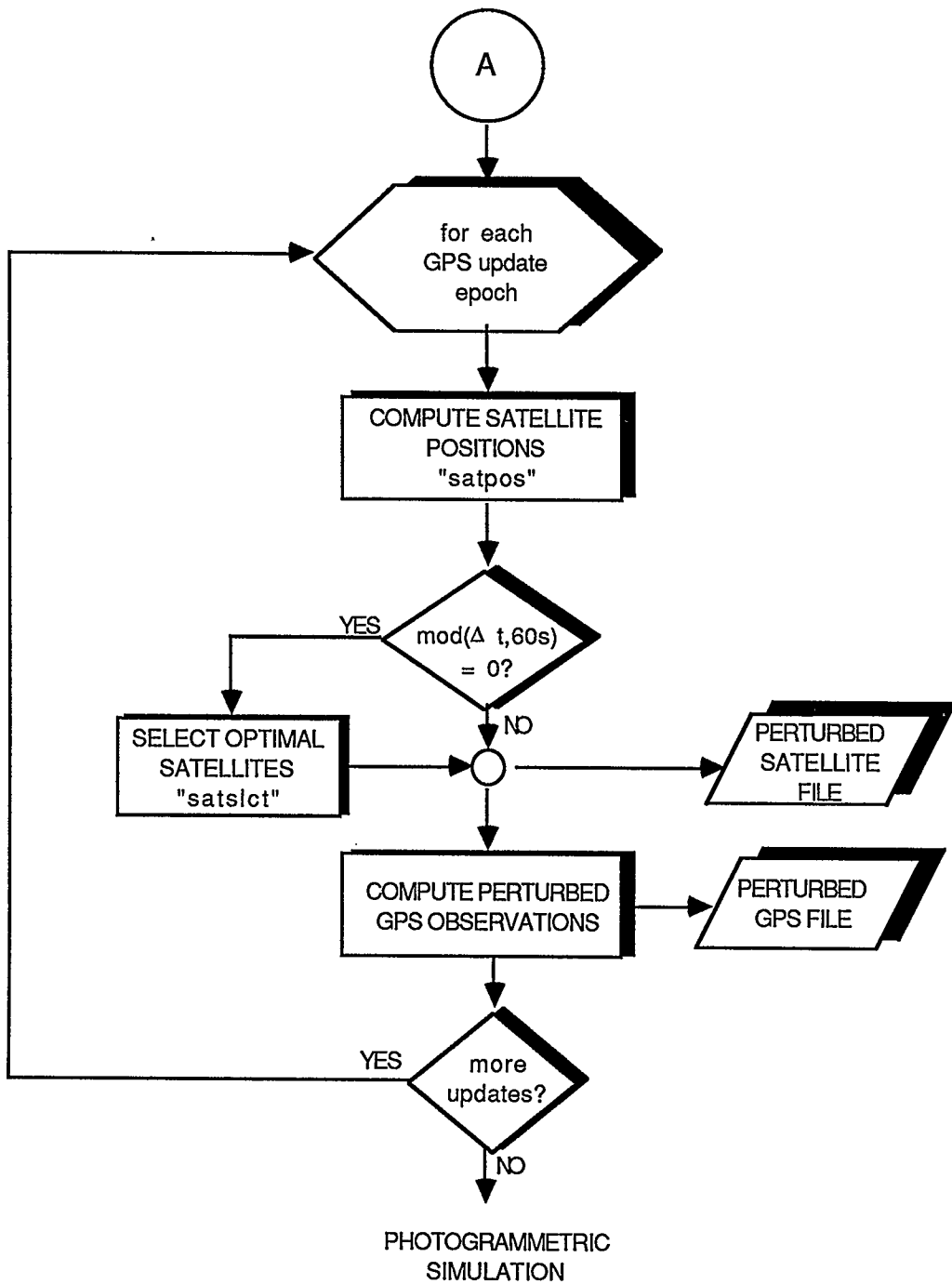
Figure 4.1b.   Simulation program "fltsim"

satellite constellation used is the one given in Fullenwider and Jorgensen (1980), but without the active spares. As mentioned above, circular orbits are simulated.

5 1

The orbital period is 43078.3 siderial seconds, and the nodes of the orbits precess at $-8.076 \cdot 10^{-9}$ s^{-1}.

4.1.6 Satellite Selection

A set of four satellites is selected each minute (but the selections change much more slowly than this). Subroutine "satslct" uses the minimum DOP criterion discussed in §3.3.1 to select four satellites. In particular, the *geometric dilution of precision* (GDOP) is used, which is the square root of the sum of all four of the diagonal elements in the normalized covariance matrix. User inputs to this process are elevation angle cutoff and maximum allowable GDOP. If the maximum GDOP is exceeded, a warning message is issued. Perturbed CT coordinates of the four selected satellites are written to a binary file at each update epoch.

4.1.7 Generation of Perturbed GPS Observations

The true ranges from the aircraft and ground receivers to each satellite are computed using the true satellite, ground, and aircraft positions. These ranges are then corrupted by tropospheric delays, ionospheric delays, and random noise. The receiver clock times are also perturbed for each update.

It has been assumed that single-frequency receivers are used. Therefore, there is no effective way to compensate for the ionospheric delay (Cannon,1987), and the entire simulated delay is an uncertainty. In order to simulate ionospheric decorrelation at the receivers, an elevation-angle-dependent single-frequency model, found for example in Martin (1980), was used. The approximate delay, in metres, is

$$\delta_{ion} = (-b \, / \, 4\pi^2 f^2) \cdot I_v \cdot \csc(E^2 + 0.126)^{1/2} \qquad (4.1)$$

52

where

> b ...is a constant which depends on fundamental physical quantities, and, in MKS units, is $1.6 \cdot 10^3$,
>
> f ...is the carrier frequency,
>
> I_v ...is the vertical electron content (electrons / m^2), and
>
> E ...is the elevation angle, in radians.

The vertical electron content I_v is a user input.

Tropospheric delays are computed using Black's approximation, which is a function of temperature, pressure, and partial water vapor pressure derived from measurements at ground level, as well as of the elevation angle E. The delay is the sum of a dry component and a wet component, and, in metres, is

$$\delta_{trop}(\text{dry}) = k_d \cdot \left\{ [1 - (\cos E / \{1 + [1 - c_l]\} \cdot d_d)^2]^{-1/2} - b_e \right\} \tag{4.2a}$$

$$\delta_{trop}(\text{wet}) = k_w \cdot \left\{ [1 - (\cos E / \{1 - [1 - c_l]\} \cdot d_w)^2]^{-1/2} - b_e \right\} \tag{4.2b}$$

$$\delta_{trop}(\text{total}) = \delta_{trop}(\text{dry}) + \delta_{trop}(\text{wet}) \tag{4.2c}$$

where

> $k_d = 1.152 \cdot 10^{-5} \cdot p \cdot [(40\,136.0 + 148.72 \cdot T) / (T + 273.16)]$,
>
> $k_w = 7.465 \cdot 10^{-2} \cdot p_{wv} \cdot [11\,000.0 / (T + 273.16)^2]$,
>
> $c_l = 0.833 + (0.076 + 1.5 \cdot 10^{-4} \cdot T) \cdot \exp(-17.188\,733\,854 \cdot E)$,
>
> $b_e = 5.848\,654\,459\,7 \cdot 10^{-4} \cdot (E^2 + 1.827\,704\,518\,6 \cdot 10^{-4})$,
>
> $d_d = (40\,136.0 + 148.72 \cdot T) / |r|$,
>
> $d_w = 11\,000.0 / |r|$,
>
> p ...is the atmospheric pressure, in millibars,

T ...is the temperature in °C,

p_{wv} ...is the partial water vapour pressure, in millibars, and

$\mathbf{r}$ ...is the geocentric position vector of the receiver, in metres.

The major uncertainty arising from the use of this formula is due to the inadequacy of surface measurements for the determination of the partial water vapour pressure along the ray path (Fell, 1980). For this reason, uncertainty in the tropospheric delay is simulated by adding a random perturbation to the input partial water vapour pressure. This error is applied only at the ground receiver, because the wet troposphere is not a significant source of error for a high-flying aircraft. The standard deviation of this perturbation is also input by the user.

Separate inputs are provided for P-code pseudorange and code measurement noise standard deviations.

4.2 Processing

Figure 4.2 illustrates the processing of the simulated observations for the two strategies used in this study. The steps used in processing the GPS and INS data are described below.

4.2.1 GPS Processing

In this study it has been assumed that the GPS receivers are able to track only four satellites, as is the case with most commercially-available equipment. Therefore, if three coordinates and a clock offset are estimated, there is no redundancy in the observations. Assuming that reasonable geometry exists, the

54
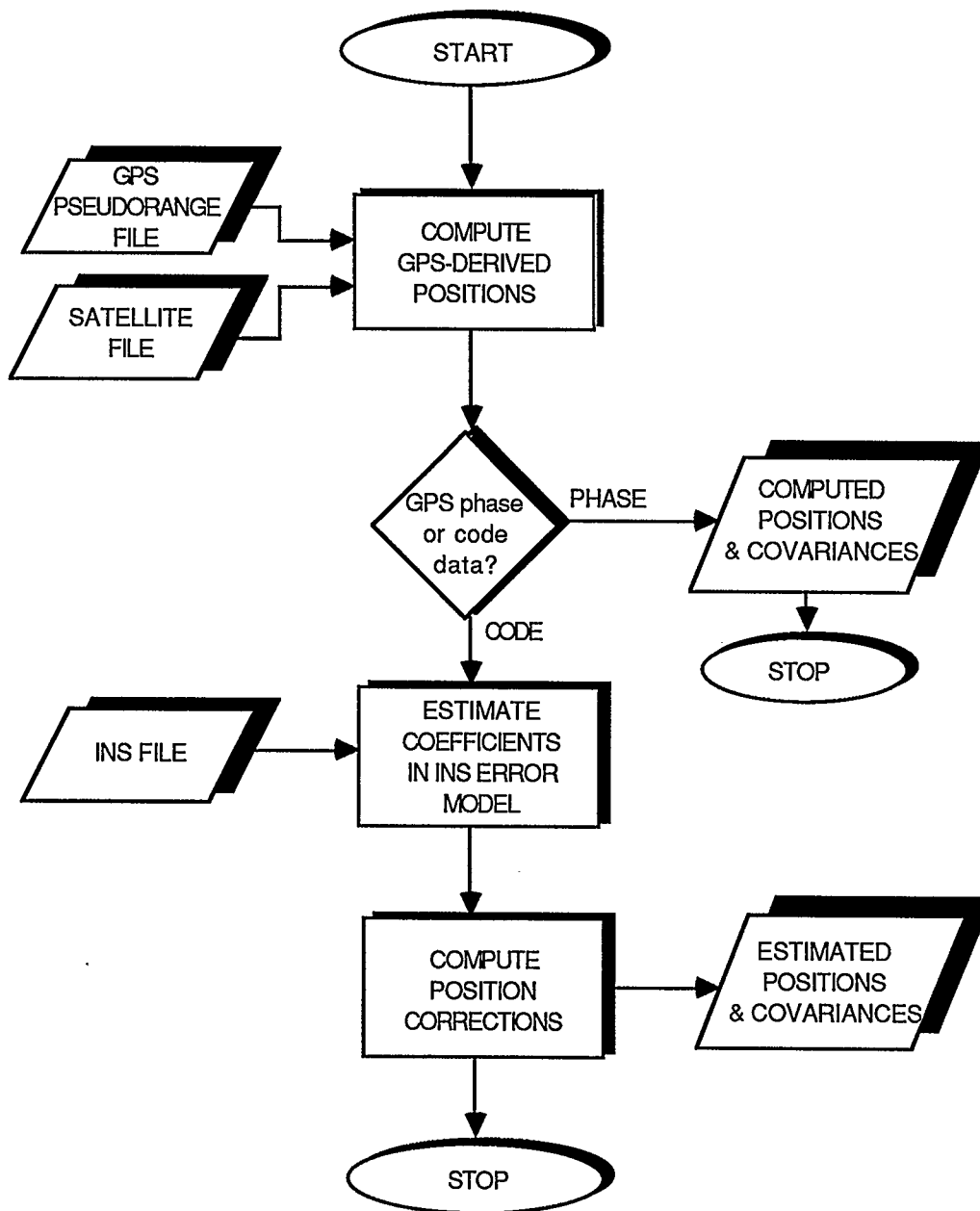
Figure 4.2. **Processing of simulated observations**

design matrices of the observations with respect to the coordinates or coordinate differences and clock bias in equations (3.30) or (3.31) are non-singular. The solution of the system of equations (3.30) can then be obtained by an iterative Taylor-

series expansion about some initial approximations, whereas the solution of (3.31) can be obtained by successive substitutions. Variances of and covariances between the coordinates and clock bias at each update epoch are approximated by equation (3.34) which, since the design matrices are non-singular, can also be written as

$$C_x = A^{-1} \cdot C_l \cdot (A^{-1})^T, \qquad (4.3)$$

In this investigation, C_l has been assumed to be diagonal, as is common practice. The computation of covariances between epochs would require a more sophisticated observation model than the one used here. Therefore, the composite covariance matrix C_x for all epochs is block-diagonal with three-by-three blocks.

For positioning strategy one, the matrices C_x are used in the estimation of INS error coefficients in equations (3.27) and their covariances. The covariances are then propagated into the estimated coordinates using (3.34). For strategy two, the matrices C_x are transformed into the photogrammetric reference coordinate system and are then used directly in the bundle adjustment along with the computed coordinates.

The remainder of the discussion on processing only applies to positioning strategy one. The use of a strapdown system in strategy two to detect cycle slips in the GPS phase data or to interpolate positions between observation epochs has not been simulated, and the actual processes were not investigated.

4.2.2 INS Processing

Equations (3.28) lead to a very simple method for estimating the error coefficients y. The least-squares estimate of these coefficients is given by

$$\langle y \rangle = -(A_I{}^T \cdot C_I{}'^{-1} \cdot A_I)^{-1} \cdot A_I{}^T \cdot C_I^{-1} \cdot dp \tag{4.4}$$

where

A_I ...is the composite design matrix for all update epochs,

C_I' ...is the covariance matrix of the observation vector, and

dp ...is the observation vector, which is composed of the differences between the GPS-derived positions and the raw INS positions.

The covariance matrix C_I' is the sum of the individual covariance matrices of the GPS and INS positions. The covariance matrix of the GPS positions, originally expressed in terms of Cartesian CT coordinates, is transformed by similarity into curvilinear coordinates for combination with the INS covariances. Therefore,

$$C_I' = C_{IG} + C_{II} \tag{4.6a}$$

$$C_{IG} = J_{\phi x} \cdot C_x \cdot J_{\phi x}{}^T \tag{4.6b}$$

where

C_{IG} ...is the covariance matrix of the GPS positions expressed in curvilinear CT coordinates,

C_{II} ...is the covariance matrix of the raw INS positions, and

$J_{\phi x}$ ...is the Jacobian matrix of the curvilinear coordinates with respect to the Cartesian coordinates.

Because the INS output is integrated, the random processes which describe the error terms ε in equations (3.27) can be nonstationary. In the simulation package described here, the position errors can be generated as either a first-order Markov process or as a random walk (Gelb, 1974). For the Markov process, an exponential correlation exists between each coordinate at adjacent epochs (resulting

in a banded matrix C_{II}), but the variances remain constant. In the case of the random walk, the matrix C_{II} is diagonal but the variances grow linearly with time. The terms in $J_{\phi x}$ can be found, for example, in Krakiwsky et al. (1977).

4.2.3 Estimation of Exposure Station Coordinates and Covariances

After the coefficients $\langle y \rangle$ have been estimated, they are used in equations (3.27) to estimate corrections $\langle \delta \lambda(t_i) \rangle$, $\langle \delta \phi(ti), \rangle$ and $\langle \delta h(t_i) \rangle$ for each *exposure* epoch, which, in general, will not occur simultaneously with the GPS updates. The estimated corrections are applied to the raw INS postitions to obtain the estimates of the exposure station coordinates. Variances of the derived coordinates are obtained using the covariance law (4.6b); in each case, the Jacobian matrix is a row vector, given by A_1^* or A_2^* in equation (3.29b).

4.3 Simulation Results

A flight pattern for a simulated photogrammetric mission was generated. This pattern is illustrated in Figure 4.3. The spacing of the lines was determined from the input photogrammetric parameters, which are discussed in Chapter 6. This same flight pattern was used for a variety of simulations incorporating up to two ground receivers and various error combinations.

Table 4.1 summarizes the parameters used in the simulations. An effort has been made to use liberal estimates of error magnitudes. This was done because, inevitably, some error sources are neglected in simulations. Estimates of actual GPS errors can be found, for example, in Martin (1980) or Payne (1982). The table is mostly self-explanatory, but a brief explanation of some of the parameters follows.
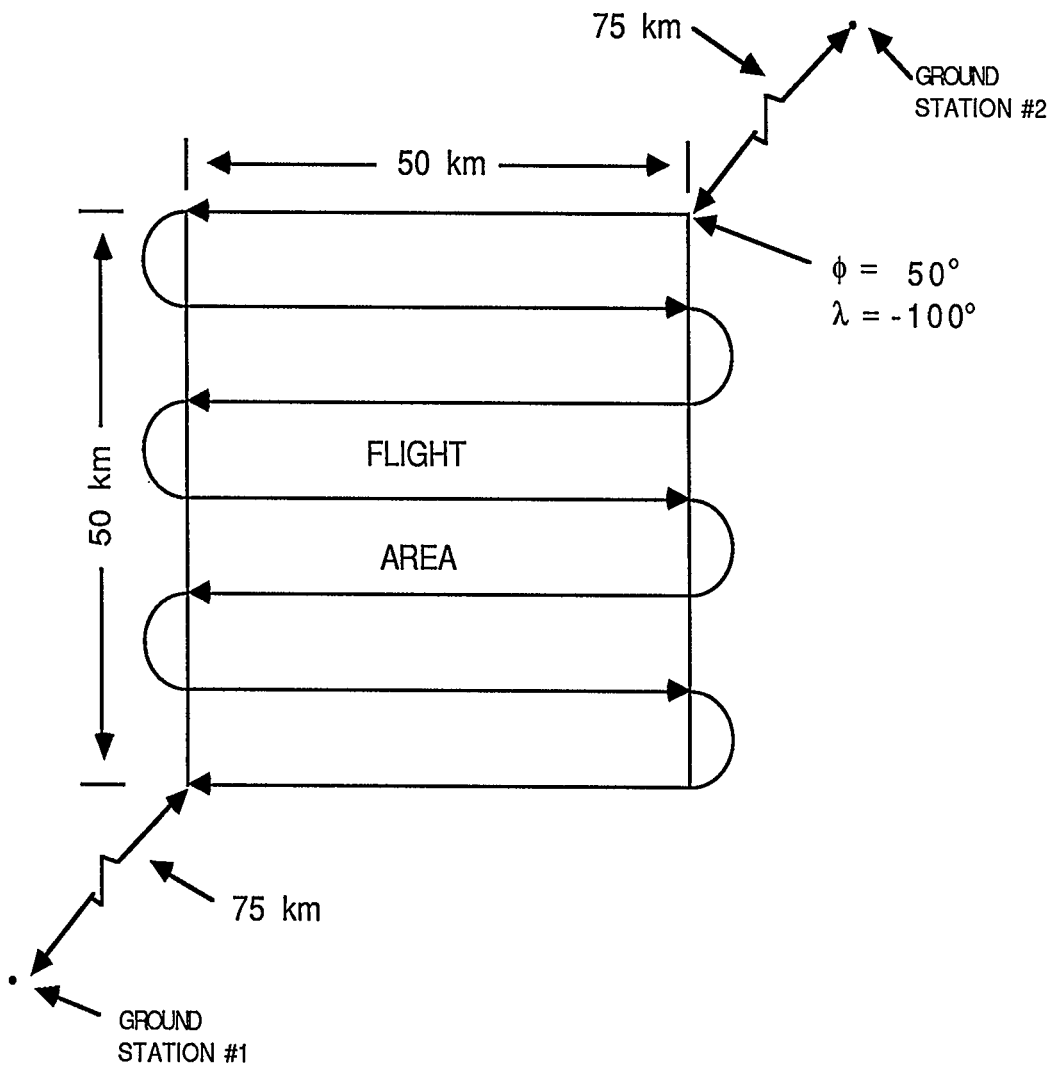
Figure 4.3.   Simulated flight pattern

The flight altitude was chosen to conform with a photography scale of 1:50 000, as is described in Chapter 6. The speed, which is reasonable for an aircraft such as a DC-3, was chosen to allow convenient synchronization of the

camera shutter with the position updates. (The shutter interval was 60 s.) This

synchronization was done strictly for simulation purposes and would not be done in

<u>Flight</u>

altitude   -   7 620 m
speed   -   76.2 m s^{-1}
duration -   5040 s

<u>GPS Utilization</u>

satellite constellation - 18 satellites in 6 orbital planes, 40° phasing,
                        55° orbital inclination
satellite selection   - 4 satellites per epoch, minimum GDOP criterion,
                        10° elevation angle cutoff
average GDOP   - 4.3
updates   - 1/3 s^{-1}, 1 680 total

<u>Errors Simulated</u>

A. Applied in all cases

    GPS code measurement noise   -   2.0 m, 1σ, uncorrelated

    GPS phase measurement noise   -   0.05 m, 1σ, uncorrelated

    GPS instantaneous clock bias   - 100 m range-equivalent, 1σ, 1st-
                                      order Markov process, 3 s cor. time
    INS system   -   grow to 5-6 kilometres in each coordinate
    INS random errors   -   0.01 m s^{-1}, 1σ, random walk in positions

B. Applied in specific cases
    orbit prediction errors (1σ, bias)
                standard   - $\Delta a = 3$ m, $\Delta i = 1.13 \cdot 10^{-7}$, $\Delta f = 1.38 \cdot 10^{-6}$
                improved - $\Delta a = 2$ m, $\Delta i = 7.53 \cdot 10^{-8}$, $\Delta f = 7.53 \cdot 10^{-8}$
    ionosphere   -   equation (4.1), $I_v = 2 \cdot 10^{17}$ m^{-2}
    wet troposphere   -   equation (4.2), 10 mb, 1σ uncertainty in p_{wv}
                          at ground receiver(s), bias

Table 4.1.   **Simulation summary**

practice. The flight duration, by coincidence, was equal to one Schuler period, which is desirable for the estimation of the INS error coefficients.

The 10° elevation angle cutoff is conservative; 5° is often used. With the 10° cutoff, some outage periods (i.e. periods with less than four visible satellites or with unacceptably high GDOP's) will occur with the 18-satellite constellation. The starting time of the simulation was chosen so that outages would not occur during the mission.

The standard orbit errors are equivalent to three metres in radius and inclination and 37 metres in the satellite anomaly. The improved (post-determined) orbit errors are based on the objectives of Krakiwsky et al. (1985) and were equivalent to two metres in each of the three perturbed elements. The ionospheric vertical electron content (I_v) of $2 \cdot 1017$ m^{-2} is a median daytime value (Martin, 1980).

Tables 4.2 and 4.3 summarize the results of the positioning simulations. Table 4.2 gives results for GPS code single-receiver and differential positioning. Table 4.3 presents results for combined GPS-INS positioning. Single-difference phase results were included in the second table to emphasize the need for cycle-slip control. The table results were obtained from five simulation runs using different random seeds. The first three figures in each table location are rms errors in ^{CT}x, ^{CT}y, and ^{CT}z, respectively. The fourth number, in parentheses, gives the standard deviation of the vector magnitudes of these errors over the five simulation runs, and is a measure of bias in the individual runs.

61

Errors / Configuration	standard orbit errors only	ionosphere only	standard orbit + ionosphere	standard orbit + ionosphere + wet troposphere	improved orbit + ionosphere + wet troposphere
Single Receiver Code	8.85 12.17 18.83 (12.05)	3.00 11.42 14.38 (0.10)	8.45 14.53 20.91 (12.31)	(no ground receiver)	3.94 11.55 17.16 (5.23)
Differential Code 1 Ground Receiver	3.23 5.55 8.46 (0.26)	3.23 5.55 8.45 (0.25)	3.23 5.55 8.46 (0.25)	3.23 5.56 8.46 (0.25)	3.23 5.55 8.46 (0.25)
Differential Code 2 Ground Receivers	2.81 4.69 7.27 (0.08)	2.81 4.69 7.28 (0.08)	2.81 4.69 7.27 (0.08)	2.81 4.69 7.27 (0.08)	2.81 4.69 7.27 (0.08)

Table 4.2.   GPS rms position errors (m)

An examination of Table 4.2 reveals that orbit prediction errors are the major source of uncertainties in single-receiver positioning.   Ionosphere uncertainties are also significant for single-receiver single-frequency operation, but could be reduced if a dual-frequency receiver is used.   For the single-receiver results, the large magnitude of the standard deviations between runs indicate that biases are present in the individual runs.   These biases are fairly large even when the improved orbit is used, and have important implications for the combination of GPS with an INS.

The most significant result in Table 4.2 is the improvement which is obtained when the differential technique is used.   The rms errors in each coordinate range from 8 to 21 metres for single-receiver pseudoranges are used, but drop to 3 to 8 metres when one ground receiver is added.   These error estimates agree with actual results given in Lachapelle et al. (1984) where standard errors of 10 to 25

metres were estimated when using a single receiver, whereas errors of 5 to 10 metres were estimated for differential positioning. Some additional improvement is obtained if a second ground receiver is added to bracket the flight area. This improvement is due to an averaging of the partially-correlated errors at the three receivers. The small values in parentheses indicate that the differential technique effectively removes the biases which are present in positions derived from single-receiver observations.

The differential results presented here were obtained by using the range-difference model of equation (3.31). An alternative method, which is applicable in real-time, uses range corrections obtained at the ground station. The pseudorange measured at the ground station is compared with the range computed from the known ground station and satellite coordinates, and the difference is transmitted to the aircraft and applied as a correction. Test results using this second method were identical to those using equation (3.31).

A common characteristic of all the results in Table 4.2 is the spatial distribution of errors. The largest errors occur in the ^{CT}z-coordinates, while the smallest occur in the ^{CT}x-coordinates. This distribution is due to the geometrical restrictions of satellite postitioning. Because all visible satellites are above the horizon, the determination of the component of position in the local vertical is weaker than the determination of the horizontal components. The northeast corner of the simulated flight pattern was placed at $(\phi, \lambda) = (50°, -100°)$. The distribution of errors in the table is due to the fact that, at this location, the local vertical has its largest projection in the ^{CT}z-axis, and its smallest projection in the ^{CT}x-axis.

The final results of the simulations for positioning strategies one and two are given in Table 4.3. The figures above the bold line pertain to strategy one, while the numbers below the line pertain to strategy two.

63

With the addition of a stable-platform INS, the accuracy of the positions derived from single-receiver pseudoranges improves only slightly, while the accuracy of positions derived from differential pseudoranges improves by an order of magnitude. This result indicates the importance of using the differential technique to reduce biases in the GPS positions. Note that preliminary results (Cannon, 1987) have not verified strategy number one, but the causes of the dis-

Errors \ Configuration	standard orbit errors only	ionosphere only	standard orbit + ionosphere	standard orbit + ionosphere + wet troposphere	improved orbit + ionosphere + wet troposphere
Single Receiver Code	8.09 10.89 16.87 (12.67)	1.79 10.58 12.96 (0.08)	7.68 13.50 19.09 (12.71)	(no ground receiver)	2.76 10.56 15.77 (5.44)
Differential Code 1 Ground Receiver	0.27 0.36 0.60 (0.13)	0.26 0.29 0.52 (0.09)	0.28 0.36 0.59 (0.12)	0.29 0.35 0.58 (0.11)	0.27 0.31 0.54 (0.06)
Differential Code 2 Ground Receivers	0.23 0.35 0.58 (0.12)	0.23 0.36 0.59 (0.11)	0.23 0.35 0.58 (0.11)	0.23 0.37 0.58 (0.15)	0.23 0.38 0.59 (0.14)
Phase Single Difference 1 Ground Receiver	0.13 0.22 0.36 (0.11)	0.12 0.15 0.22 (< 0.01)	0.16 0.24 0.36 (0.09)	0.16 0.26 0.33 (0.18)	0.13 0.22 0.29 (0.08)
Phase Single Difference 2 Ground Receivers	0.07 0.12 0.20 (< 0.01)	0.07 0.12 0.18 (< 0.01)	0.08 0.12 0.20 (< 0.01)	0.08 0.21 0.29 (0.09)	0.08 0.21 0.27 (0.09)

Table 4.3.   GPS-INS rms position errors (m)

crepancies have not yet been identified.

The highest accuracies were obtained by using GPS phase observations. Again, these simulation results are in line with recent field test results obtained by

Schwarz et al. (1987), in which estimated errors were between 0.1 to 0.5 metres in each coordinate for cycle-slip free data. Cycle-slip control is still needed, however. The GPS phase technique is attractive because an inexpensive strapdown INS can be used for this purpose. The GPS phase results improved slightly when a second ground receiver was added. The addition of a second receiver may also be desirable to increase the system reliability with regards to ambiguity resolution and cycle slips.

As a check on the simulation results, the propagated coordinate covariances were compared with the rms coordinate errors. As would be expected, the covariance estimates agreed with the coordinate errors when systematic effects were not present, but they were too optimistic when such effects were simulated.

Again, it should be mentioned that the strapdown INS was not simulated, and that the phase results presented were obtained simply by replacing the code observations (which were used to generate Table 4.2) with more precise phase observations. The details of cycle-slip detection and correction have yet to be worked out.

Chapter 5

Aerotriangulation Concepts and Models

This chapter will introduce photogrammetric concepts and will describe math and error models for aerotriangulation. In Chapter 6, the simulation and processing of photogrammetric observations is described, and simulation results are presented.

5.1 Aerotriangulation Concepts

The ultimate aim of this study is to develop methods to reduce the difficulty and expense of topographic mapping. One of the key steps in making maps from aerial photographs is *aerotriangulation*. The object of aerotriangulation is to determine the coordinates of points on the ground by exploiting ray intersections in overlapping aerial photographs. The earliest applications of photogrammetry used analog means to produce maps from photographs. Thus, in its original form, aerotriangulation was strictly an optical-mechanical procedure. As the science developed, photogrammetric equipment (primarily stereoplotters) became more sophisticated, as did the techniques used to exploit the information in the photographic imagery. Analytical techniques became a key element in the mapping process with the advent of the digital computer in the late 1950's (Brown, 1976). The most important trend today is the supplanting of photographic imagery with digital imagery. Mechanical procedures, however, are still prevalent in the mapping industry.

Techniques and terminology in photogrammetry are inextricably tied to its historical development. Hence, some of the methods and language used today may seem obsolete in the context of today's digital technology (Rauhala, 1987). It is instructive, however, to examine a traditional sequence of operations in order to understand the nature of the photogrammetric problem. In stereoplotters, the mapping process can be divided into four distinct steps: interior orientation, relative orientation, absolute orientation, and compilation.

The purpose of interior orientation is to recreate the internal geometry and conditions of the camera at the time of exposure. Roughly defined, the elements of interest include the *principal distance*, or the perpendicular distance from the camera's perspective centre to the image plane, the location in the image plane of the *principal point*, which lies at the foot of the perpendicular from the perspective centre, and parameters of lens distortion.

Interior orientation is facilitated in aerial mapping by the use of *metric* cameras. A metric camera is "a camera whose interior orientation is known, stable, and reproducible" (ASP, 1980). The elements of interior orientation are determined in laboratory precalibration and are generally assumed to be constant between calibrations. This assumption, however, is not justified in practice (Brown, 1985), as will be discussed in §5.3. Metric cameras are provided with reference marks, known as *fiducials*, which are imaged in each exposure. Usually, four to eight fiducials are distributed around the periphery of the image, as shown in Figure 5.1. Some cameras are equipped with a *reseau*, which is a grid of reference marks distributed throughout the image plane. The purpose of these reference marks is to establish a reproducible photocoordinate system to which all photogrammetric observations refer. The marks, especially reseau, are also used in the compensation of some image-variant effects, such as film shrinkage and unflatness of the image

plate. Analog procedures for interior orientation include the setting of the calibrated principal distance, the alignment of the photographic transparency in the projector carriage, and the correction of lens distortion by compensating optics. Today these operations have almost universally been replaced by mathematical techniques. Although interior orientation can be integrated with relative and absolute orientation in a unified aerotriangulation, it is usually performed as a separate process.
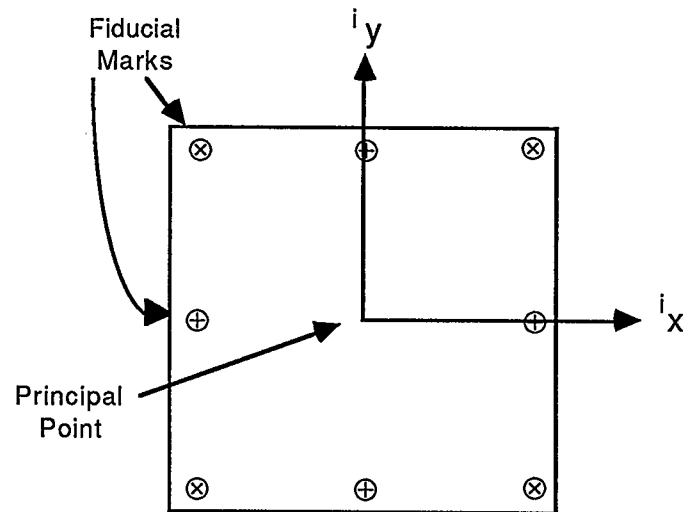
Figure 5.1.   Fiducials and photocoordinate system

In relative orientation, the spatial relationship of a pair of exposures is reproduced, creating the *stereomodel* (Wolf, 1974). The stereomodel is the locus of conjugate ray intersections from a pair of relatively-oriented photographs. A ray intersection from a pair of conjugate images is illustrated in Figure 5.2. The coordinate systems in the figure are discussed in §5.2. The stereomodel reproduces the shape of the imaged object (in this case terrain), but the scale and orientation of the model are arbitrary. In mechanical plotters, relative orientation is done by physical

translations and rotations of the projectors. Mathematically, relative orientation involves the determination of five quantities chosen from the 12 spatial degrees of freedom of the two projectors.

During absolute orientation, the scale and orientation of the stereomodel with respect to a reference coordinate system are determined. Again, in analog plotters, this is accomplished by moving the projectors so that the rays corresponding to ground control points intersect at pre-determined locations in the map volume. An analytical solution requires that seven additional parameters be determined, thus accounting for the total of 12 degrees of freedom of the projectors.
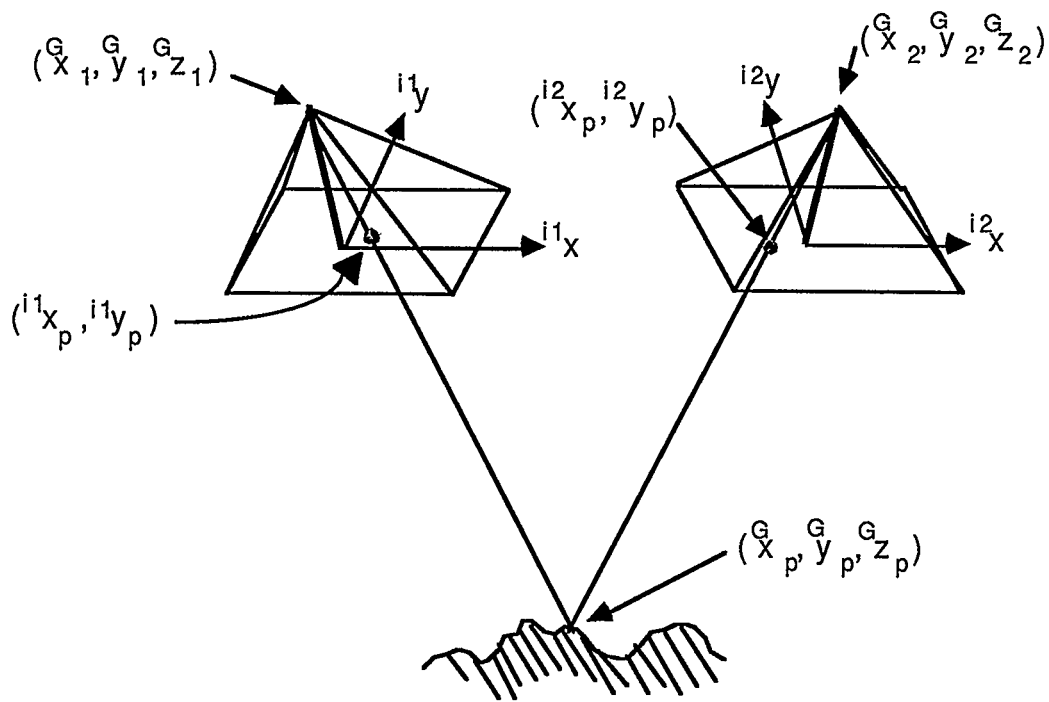
Figure 5.2. Conjugate images and ray intersection

Relative and absolute orientation are together called *exterior orientation.* There are six elements of exterior orientation per photo; these are the three spatial coordinates of the exposure stations along with three orientation parameters which relate the ground coordinate system to the photocoordinate system. Once exterior orientation has been completed, the map compilation process can begin. Mechanically, compilation involves the tracing of features and topography by an operator. Although automated terrain compilation has been around for a number of years (Kok, 1986) and is becoming more prevalent, manual compilation is still almost universal.

So far in this discussion, explicit consideration has been given only to pairs of photographs. The use of pairs of photographs without regard to other photographs in the mapping area is restrictive, however, because at least three ground control points must appear in each pair, and because large discontinuities may appear between adjacent pairs. These restrictions motivated the development of a technique called *bridging.* Using this technique, control can be extended to models in which no ground control was established. Mechanical bridging was implemented by using multiple projectors, by imposing constraints on the projector movements in so-called *universal* stereoplotters, or by radial-arm triangulation, which is a form of analog least-squares adjustment (ASP, 1980). With the introduction of digital computers, analytical bridging in large blocks of photographs, or *block adjustment*, became feasible.

Figure 5.3 illustrates a block of 24 photographs and a typical ground control configuration. Each rectangle is, roughly, the overlap area between two adjacent photographs in a strip. The shaded areas are overlap between adjacent strips. The amount of overlap determines the number of photographic ray intersections which occur at each ground point. Typical values are 60% end lap (in

70

strip direction) and 30% side lap (between strips), which results in three to six ray intersections per point. Increasing the amount of overlap enhances the reliability and precision of aerotriangulation (Lucas, 1984), but it also increases the expense.
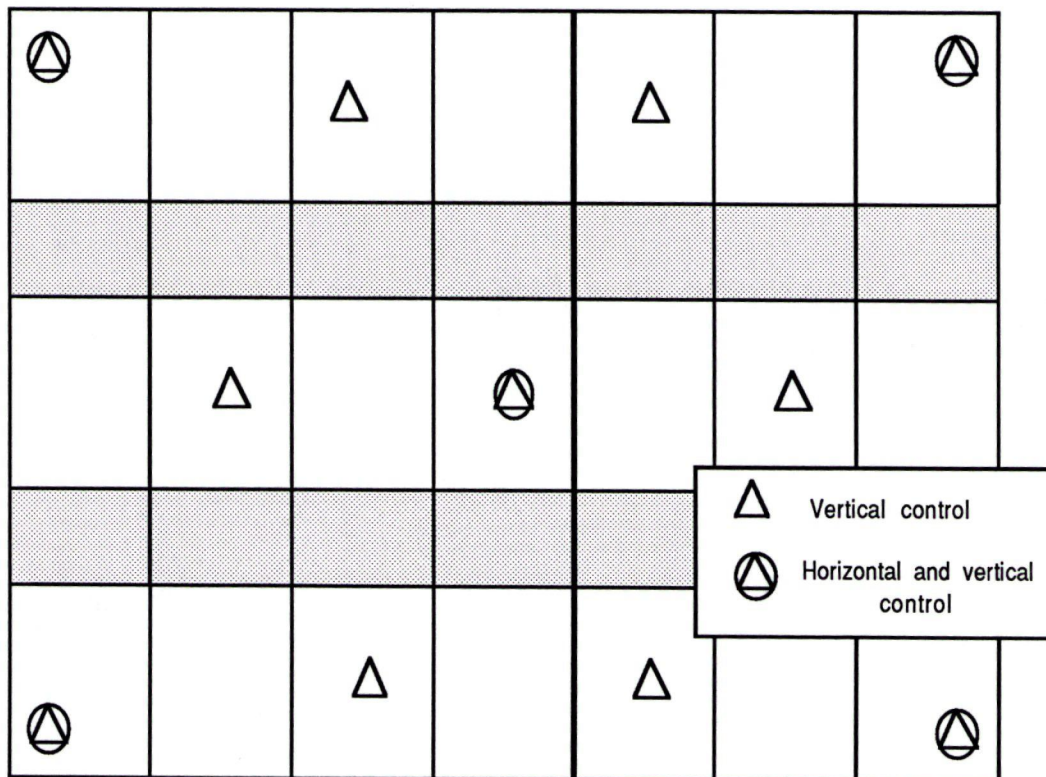
Figure 5.3.   Typical ground control configuration

Conceptually, the block may be thought of as a sheet of plastic, and the control points can be viewed as tacks which constrain the sheet's horizontal or vertical movements with respect to the ground coordinate system. The control points can be conspicuously marked on the ground, or pre-targeted, before the area is flown, or, alternately, they can be established on well-defined features which

71

appear on existing photography. Control is extended photogrammetrically to other points on the ground so that there are several points in each model. These new points, known as *tie points*, must be well-defined so that they can be identified in each photograph in which they appear. Tie points constrain the block's internal deformations. In this study, ground control has been replaced by control at the exposure stations, such as $(^Gx_1, {}^Gy_1, {}^Gz_1)$ and $(^Gx_2, {}^Gy_2, {}^Gz_2)$ in Figure 5.2, and all points identified in the imagery are tie points. Note that the "sheet of plastic" is less constrained with exposure station control, as will be seen below. Although tie points can also be pre-targetted, it has been assumed here that they have not been marked. Thus, it is not necessary for anyone to enter the area to be mapped.

There are several different types of analytical block adjustment in use. In *independent model block adjustments* (Blais, 1979), relative and absolute orientation are performed separately. In this study, a *bundle adjustment* (Brown, 1976) was used, in which relative and absolute orientation are combined. The word "bundle" refers to the bundles of rays which create each image. The bundle adjustment was selected because it permits the rigorous incorporation of a priori covariance information on the exposure station coordinates, ground station coordinates, and photocoordinate measurements. In *self-calibrating bundle adjustments*, parameters of interior orientation may also be recovered (ibid.). Self calibration was not used in this investigation.

Mapping from aerial photography is usually done with vertical photography, and deviations of the camera's optical axis of only two or three degrees from the vertical are allowed. Vertical photography was (and still is) used because of restrictions of the human visual system which constrain stereoplotter design, and because it simplifies the mathematics. A consequence of vertical photography is that the determination of the heights of ground points is somewhat

weaker than the determination of horizontal coordinates. In this study, vertical photography is assumed.

5.2 Aerotriangulation Model

Two new coordinate systems are introduced. The photocoordinate system is shown in Figure 5.1. The axes in the figure are only approximate, as the exact directions of these axes with respect to the fiducial marks is determined in laboratory precalibration. For the case of vertical photography, the ^ix-axis nearly coincides with the direction of flight, known as the *epipolar* direction. The origin of the system is at the interior nodal point, which is treated as the perspective centre (Merchant, 1973). As a first approximation, image points are constrained to a plane, and thus all image points have a constant ^iz-coordinate equal to the camera principal distance. For aerial cameras focussed at infinity, the principal distance is equal to the focal length of the lens. The ^iy-axes completes the right-handed system.

The ground coordinate system used in this study is a three-dimensional Cartesian system. Its origin is on the ellipsoid at the centre of the flight area, its xy-plane is tangent to the ellipsoid at the origin, its x-axis points east, and its y-axis points north to complete the right-handed system. This system is equivalent to a local-level system, such as that illustrated in Figure 3.1, with its origin at the map centre. Ground coordinates are designated by the superscript "G".

The basic observation model for aerotriangulation is known as *collinearity*, which is the condition that the ground point, the cameras perspective centre, and the image of the ground point lie on a straight line. In the literature, the collinearity equations are usually derived using geometric optics with a thin lens (ASP, 1980). Bender (1971), however, wrote an interesting dissertation in which

73

the equations were derived by imposing constraints on the general projective equations. With reference to Figure 5.2, the observation equations are given by

$$^{in}x_p = {}^{in}x_{pp} - f \cdot \frac{x'}{z'} + \delta x_{lens} + \delta x_{at} + \varepsilon_x \tag{5.1a}$$

$$^{in}y_p = {}^{in}y_{pp} - f \cdot \frac{y'}{z'} + \delta y_{lens} + \delta y_{at} + \varepsilon_y \tag{5.1b}$$

where

$^{in}x_p, {}^{in}y_p$ ...are photocoordinates of the image of point p in photo n,

$^{in}x_{pp}, {}^{in}y_{pp}$ ...are principal point offsets from precalibration,

f ...is the camera principal distance from precalibration,

$\delta x_{lens}, \delta y_{lens}$ ...are computed corrections for lens distortion,

$\delta x_{at}, \delta y_{at}$ ...are computed corrections for atmospheric refraction,

$\varepsilon_x, \varepsilon_y$ ...are due to unmodeled effects, and

x', y', z' ...are components of the vector from exposure station n to ground point p expressed in the photocoordinate system.

The vector (x', y', z') is given by

$$\begin{bmatrix} x' \\ y' \\ z' \end{bmatrix} = {}^{in}R_G \cdot \begin{bmatrix} {}^Gx_p - {}^Gx_n \\ {}^Gy_p - {}^Gy_n \\ {}^Gz_p - {}^Gz_n \end{bmatrix} \tag{5.2}$$

where $^{in}R_G$ is a direction cosine matrix which rotates from the ground coordinate system into the photocoordinate system of photo n, and the other coordinates are as illustrated in Figure 5.2.

The parameters f, $^{in}x_{pp}$, and $^{in}y_{pp}$ are known as the *primary elements of interior orientation*, and the fact that they are determined in laboratory precalibration has significant implications in this study, as will be seen below. Note that there are several different definitions for the principal point. The offsets $^{in}x_{pp}$, and $^{in}y_{pp}$ are the photocoordinates of the *principal point of minimum variance* (Merchant, 1973).

5.3 Aerotriangulation Error Model

The error terms ε_x and ε_y in equations (5.1) are due to inadequacies of the various precalibration models, uncertainties in the parameters determined in precalibration, neglected effects such as film shrinkage and film unflatness, and residual atmospheric uncertainty. In this study the most significant effects are variations in the primary elements of interior orientation, and these were the only errors which were explicitly simulated. For the sake of completeness, however, a short discussion of other error sources precedes the treatment of the latter errors.

5.3.1 Lens Distortion

Deviations from collinearity due to lens distortion are primarily due to two physical phenomena:

1. departures of the lens surfaces from their ideal shape (a parabaloid of revolution), and

2. non-alignment of the various elements of the compound lens

(Merchant, 1973). Distortion due to the former cause is known as *radial distortion*, while that due to the latter is known as *decentering distortion*. The models which

75

are most commonly used to compute these effects are due to A.E. Conrady, who published his work in 1919 (ibid.). Radial distortion is usually modeled as an odd-powered polynomial in the radial image distance, i.e.

$$\Delta r_{rad} = a_1 \cdot r + a_2 \cdot r^3 + a_3 \cdot r^5 + \ldots \qquad (5.3a)$$

$$r = ({}^i x^2 + {}^i y^2)^{1/2} . \qquad (5.3b)$$

As an alternative, Munjy (1986) has suggested using a variable focal length represented by finite elements in the image plane, thus eliminating the assumption of radial symmetry implicit in (5.3).

Conrady's model for decentering distortion is of the form

$$\Delta r_{dec} = 3 \cdot P(\mathrm{r}) \cdot \sin(\phi - \phi_0) \qquad (5.4a)$$

$$\Delta t_{dec} = P(\mathrm{r}) \cdot \cos(\phi - \phi_0) \qquad (5.4b)$$

where

$\Delta r_{dec}, \Delta t_{dec}$	…are radial and tangential components of decentering distortion,
ϕ	…is the angle to the image point radius vector in the image plane,
ϕ_0	…is the direction of maximum tangential distortion, and
$P(r)$	…is an even-powered polynomial in r

(Fryer and Brown, 1986).

In self-calibrating adjustments, a subset of the coefficients in equations (5.3) and (5.4) are recovered along with the other unknown parameters. In laboratory calibration, the convention is to provide distortion values in table or

76

graph format, leaving the choice of interpolation method to the user. Piecewise-linear interpolation is usually effective (Chapman, 1987). For modern aerial cameras, residual uncertainties in lens distortion are below the noise level of most photogrammetric instruments. Therefore, these effects have not been explicitly treated in this investigation.

5.3.2 Atmospheric Refraction

Refraction in aerial photography is due to the variation of air density in the atmosphere. As a first approximation, it can be assumed that atmospheric density is strictly a function of altitude, and, therefore, that vertical rays are not deflected. Consequently, for vertical photography, atmospheric refraction is usually computed as a function of radial image distance using

$$\Delta r = K \cdot \left(r + \frac{r^2}{f^2} \right) \tag{5.5}$$

where K is an empirical function of altitude (ASP, 1980). The slight deviations of near-vertical photography from true verticality do not induce significant errors in the computed values (Merchant, 1973). For a standard 6-inch focal length, nine-inch format camera and a flying height of 7600 metres, the computed image displacement due to atmospheric refraction can reach 24 micrometres at the corners of the photo. Residual uncertainties, however, are below the noise level of photogram-metric measurements, and refraction has not been simulated in this study.

5.3.3 Other Image-Variant Effects

There are several distortions which do not have explicit representation in equations (5.1). The most significant of these are due to film shrinkage and unflatness of the film during exposure. The effects of film shrinkage, and, to a lesser extent, film unflatness can be reduced by use of a reseau. Brown (1976), however, found significant residual systematic errors caused by deformations of the reseau-carrying platen itself, and these findings resulted in the design of a new platen. It has been assumed that such a non-deforming platen was used for the photography in this study, and film shrinkage and unflatness have not been explicitly treated.

5.3.4 Projective Compensation

For metric cameras, the primary elements of interior orientation - f, $^{in}x_{pp}$, and $^{in}y_{pp}$ - are determined in laboratory precalibration. Aerial cameras, however, are operated under a variety of environmental conditions, and these elements can not be assumed to remain constant. Variations of 50 micrometres in f and 3 micrometres in $^{in}x_{pp}$ and $^{in}y_{pp}$ can occur (Brown, 1985). If all control is at ground level, the variations in the primary elements do not contribute significant uncertainties to aerotriangulated ground coordinates due to a phenomenon called *projective compensation*. Conversely, when ground control is replaced by exposure station control, the consequences of projective compensation are detrimental.

Projective compensation is a consequence of coupling between certain parameters in the collinearity equations. Of concern here is the coupling between the primary elements of interior orientation and the ground and exposure station coordinates. This phenomenon can be readily understood by making the

simplifying assumtions that the photography is truely vertical and that the horizontal axes are in alignment with the ground axes. In this case, $^{in}\mathbf{R}_G \to \mathbf{I}$ in equation (5.2) and equations (5.1) become (neglecting error terms)

$$^{in}x_p = {}^{in}x_{pp} - f \cdot \frac{{}^{G}x_p - {}^{G}x_n}{{}^{G}z_p - {}^{G}z_n}$$

(5.6a)

$$^{in}y_p = {}^{in}y_{pp} - f \cdot \frac{{}^{G}y_p - {}^{G}y_n}{{}^{G}z_p - {}^{G}z_n}.$$

(5.6b)

An examination of these equations reveals that there is coupling between the following pairs of elements: $^{in}x_{pp} \leftrightarrow {}^{G}x_p$, $^{in}x_{pp} \leftrightarrow {}^{G}x_n$, $^{in}y_{pp} \leftrightarrow {}^{G}y_p$, $^{in}y_{pp} \leftrightarrow {}^{G}y_n$, $f \leftrightarrow {}^{G}z_p$, and $f \leftrightarrow {}^{G}z_n$. This coupling is indicated by the fact that the ratios of partial derivatives of equations (5.6) with respect to each member of the pairs is equal to $\pm f / ({}^{G}z_p - {}^{G}z_n)$. For most aerial photography, $^{G}z_n \gg {}^{G}z_p$ for all points p, and this ratio is practically constant. This near-perfect linear dependence of these elements precludes the estimation of both members of any pair for vertical photography over relatively flat terrain (Merchant, 1973). Therefore, the determination of $^{in}x_{pp}$, $^{in}y_{pp}$, and f by self-calibration is not feasible in this study.

When all control is at ground level, errors in the primary elements of interior orientation are "soaked up" by the exposure station coordinates $^{G}x_n$, $^{G}y_n$, and $^{G}z_n$. This effect is most pronounced in the coupling $f \leftrightarrow {}^{G}z_n$, which has a similar contribution from both equation (5.1a) and equation (5.1b). Since the exposure station coordinates are essentially "nuisance parameters" in aero-triangulation, projective compensation results in beneficial effects for ground-controlled block adjustments. When the exposure station corrdinates are cons-

79

trained, however, errors in the interior orientation elements propagate into the ground coordinates, which are the parameters of interest. For this reason, errors in $^{in}x_{pp}$, $^{in}y_{pp}$, and f were simulated, as is discussed in Chapter 6.

Chapter 6

Photogrammetric Simulation, Processing, and Results

The trajectory simulation discussed in Chapter 4 was used to drive a photogrammetric simulation. The generation of photogrammetric data and the use of these data and the simulated exposure station positions in a bundle adjustment are described in this chapter, and simulation results are presented.

6.1 Photogrammetric Simulation

Figure 6.1 is a simplified flowchart of the photogrammetric simulation. Some of its features are discussed below.

6.1.1 Photogrammetric Input

Photogrammetric data comprises part of the input to the simulation program "fltsim". The camera focal length, along with the percentage of end and side overlap, determines the spacing of the flight lines and the exposure and GPS update intervals. Other input parameters are standard deviations of camera orientation elements from true verticality and from azimuthal alignment with the ground coordinate system, amount of relief variation for tie points, and standard deviations of the primary elements of interior orientation and of photocoordinate measurements.

TRAJECTORY
SIMULATION

PHOTOGRAMMETRIC
INPUT

PERTURB INTERIOR
ORIENTATION
ELEMENTS

for
each
image

GENERATE NEW
TIE POINT GROUND
COORDINATES

GROUND
"TRUTH"
FILE

GENERATE PERTURBED
IMAGE COORDINATES

PERTURBED
IMAGE
FILE

YES

more
images?

NO

STOP
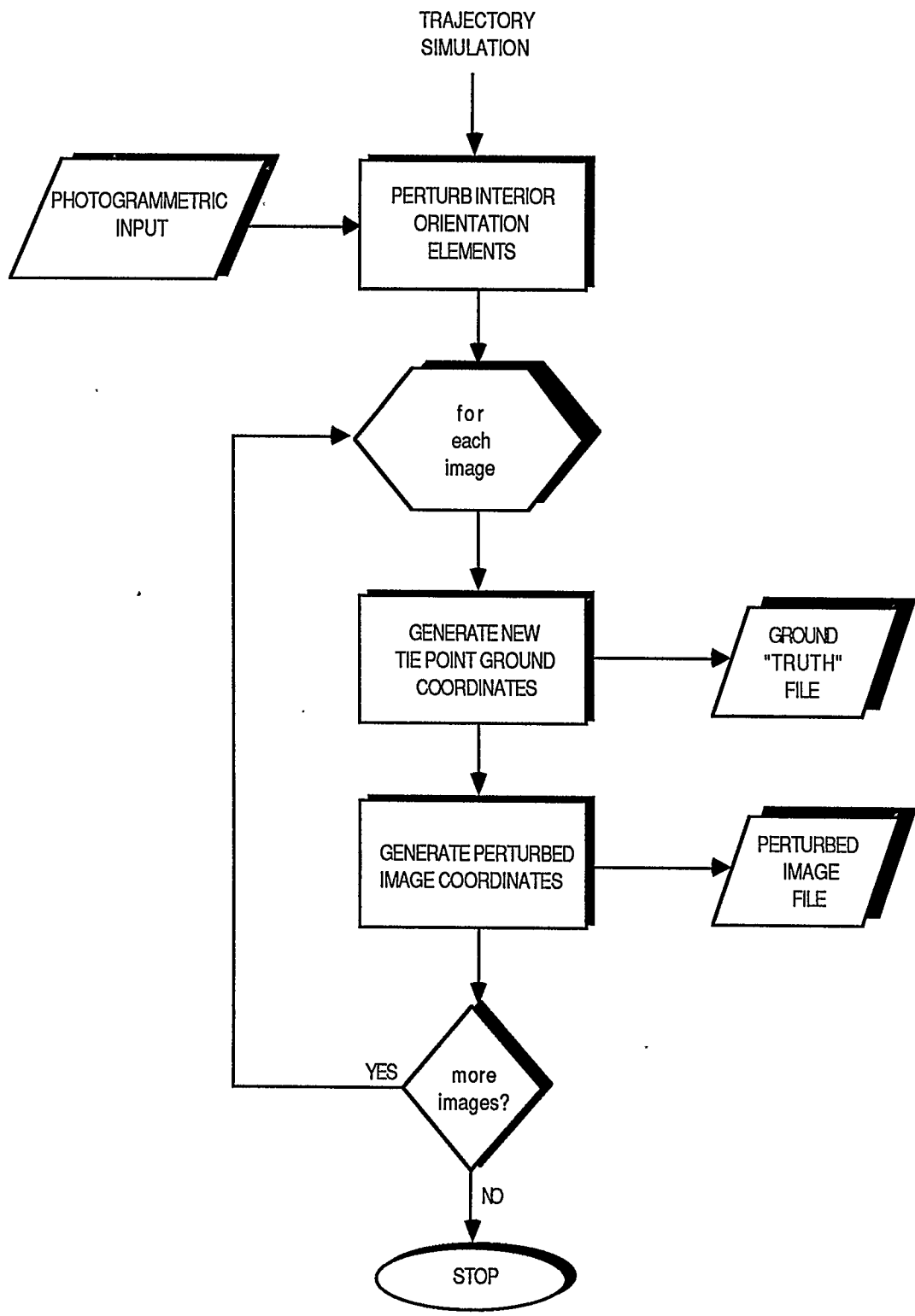
Figure 6.1.   Photogrammetric simulation

6.1.2 Perturbation of Interior Orientation Elements

The focal length and principal point coordinates are given random perturbations based on the input standard deviations. These perturbed elements are held constant for the duration of the simulation run.

Figure 6.2.   Tie point configuration

6.1.3 Generation of Tie Points

Figures 6.2 and 6.4 illustrate the tie point configuration used. Nominally, nine tie points are generated per image. In Figure 6.2, six photos from the interior

of the block are shown. The small squares indicate tie points near the principal points of each of the six photos. The photos have been offset in the figure to illustrate the overlap. The tie points along the line connecting the principal points are imaged in three photos and thus are determined by three ray intersect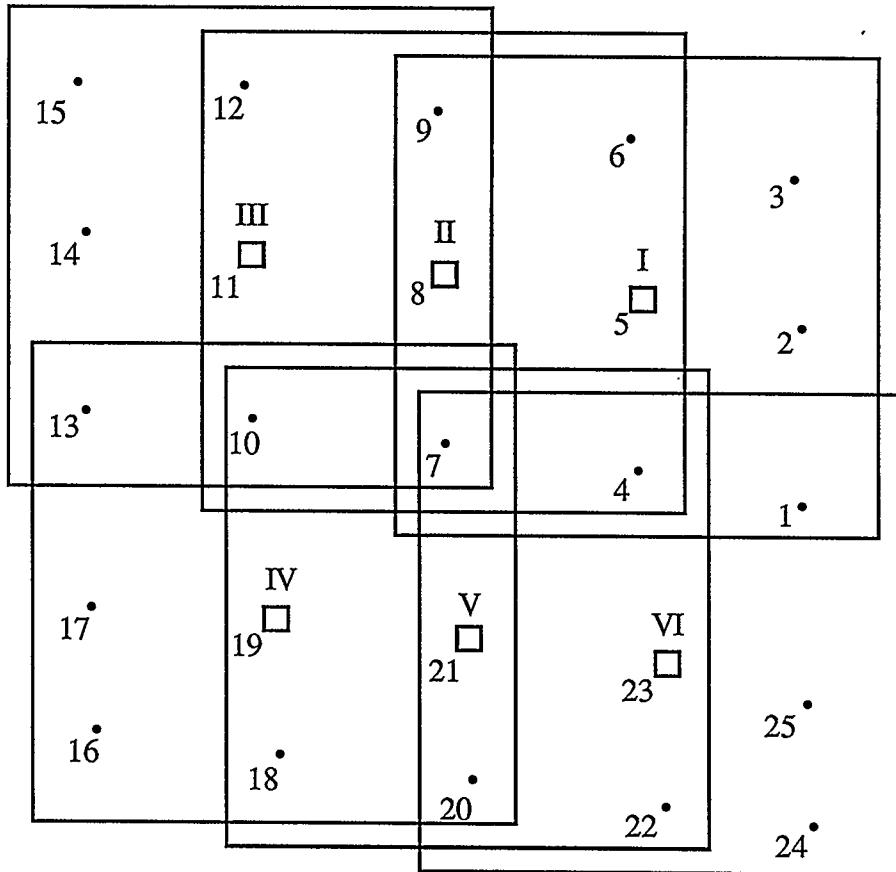ions, while the points near the edges of the photos are determined by six ray intersections. As shown in Figure 6.4, no tie points are generated at the ends of the flight lines. Relief is generated in a regular pattern using the input terrain parameter.

6.1.4 Generation of Image Coordinates

Image coordinates are generated for each tie point in the image using equations (5.1) and the perturbed interior orientation elements. For each image, the camera is given a random orientation with respect to the ground coordinate system. The deviations in orientation are based on values input by the user. The image coordinates are given additional random errors based on input standard deviations.

6.2 Photogrammetric Processing: The Bundle Adjustment

In its most simple form, the bundle adjustment is a combined relative and absolute orientation of a block of overlapping photographs. The parameters to be determined are six exterior orientation elements for each photo and three ground coordinates for each tie or control point. The choice of the three angular exterior orientation elements is arbitrary (Merchant, 1973). *Gimbal angles* are the most common choice, and they have been used here. These are three sequential rotations of the ground system into the photocoordinate system: ω, a rotation about the x-axis, ϕ, a rotation about the (new) y-axis, and κ, a rotation about the (new) z-axis. Sometimes the order of these rotations is changed, resulting in different numerical

values for these parameters. The rotation matrix $^{in}\mathbf{R}_G$ in equation (5.2), however, is unique, regardless of the parameterization.

Two types of observation equations are used. The first is the collinearity condition (5.1) which relates the exterior orientation elements and ground coordinates to photocoordinate observations. The second observation type incorporates a priori information on the parameters which are to be estimated. This second model is of the simple form

$$\mathbf{x} = \mathbf{x}_0 + \mathbf{\varepsilon}_{x0} \qquad (6.1)$$

where

$\mathbf{x}$ ...is the vector of parameters (exterior orientation elements and ground coordinates),

$\mathbf{x}_0$ ...are initial estimates of the parameters, and

$\mathbf{\varepsilon}_{x0}$ ...is a random vector with zero mean with associated covariance matrix $\mathbf{C}_{x0}$.

In this study, the matrix $\mathbf{C}_{x0}$ takes the form

$$\mathbf{C}_{x0} = \begin{bmatrix} \mathbf{C}_{xpc} & \mathbf{0} \\ \mathbf{0} & \mathbf{C}_{xG} \end{bmatrix} \qquad (6.2)$$

where $\mathbf{C}_{xpc}$ is block diagonal with 6×6 submatrices composed of the covariances of the perspective centre coordinates (computed as described in Chapter 4) and the a priori variances of the perspective centre gimbal angles, and $\mathbf{C}_{xG}$ is diagonal and composed of the a priori variances of the tie point ground coordinates. The collinearity equations are linearized by a first-order Taylor series expansion. Utilizing both types of observations, the least-squares solution for the parameters is

$$\langle \delta x \rangle = -\left(A^T \cdot C_l^{-1} \cdot A + C_{x0}^{-1}\right)^{-1} \cdot A^T \cdot C_l^{-1} \cdot w \qquad (6.3)$$

where

$\langle \delta x \rangle$ ...is a vector of estimated corrections to the approximate parameters x_0,

A ...is the design matrix arising from the collinearity condition,

C_l ...is the covariance matrix of the observed photocoordinates (assumed here to be diagonal), and

w ...is the misclosure vector composed of the differences between the observed photocoordinates and the photocoordinates computed using the parameter estimates

(Krakiwsky, 1982). The solution is iteratively improved until it satisfies a convergence criterion. Note that some of the variances in C_{x0} may be very large, as were the gimbal angle variances and the tie point coordinate variances C_{xG} in this study. Nevertheless, the corresponding weights are often used in the solution (6.3), even though they are very small. These weights are useful, however, since the addition of small quantities to the main diagonal of the coefficient matrix increases the numerical stability of the system.

For a block of aerial photographs, the system of normal equations can be quite large. For the relatively small block of photographs used in this study (48 photos and 108 tie points), there are 288 exterior orientation parameters and 324 ground coordinates to be estimated. The solution of the resulting 612×612 system of equations by brute force is not practical. Fortunately, with proper parameter ordering, the normal equations have a sparse pattern which is easily exploited. The

usual scheme is to order the photo unknowns first and the ground coordinates second. The normal coefficient matrix then assumes the form

$$A^T \cdot C_l^{-1} \cdot A + C_{x0}^{-1} = N = \begin{bmatrix} N_{11} N_{12} \\ N_{12}^T \ N_{22} \end{bmatrix} \qquad (6.4)$$

where N_{11} corresponds to the exterior orientation elements and is block-diagonal with symmetric 6×6 blocks, N_{22} corresponds to the ground coordinates of the tie points and is block diagonal with symmetric 3×3 blocks, and N_{12} is a sparse matrix.

Figure 6.3 is a schematic of the structure of a portion of the normal coefficient matrix corresponding to the six photos and 25 tie points illustrated in Figure 6.2. The shaded sections are the locations of non-zero elements. The numerical ordering shown in Figure 6.2 was used, with the exterior orientation parameters of the six photos (in the order indicated by the Roman numerals) coming first, and the tie points (in the order indicated by the Arabic numerals) coming second. For any configuration there is a particular parameter ordering which minimizes the bandwidth of the matrix. The ordering shown in the figure is not optimal, but it is similar to the ordering used in this study. Optimal ordering would not have improved the efficiency of the bundle adjustment in this research, however, because a relatively simple partitioning and solution scheme was used. Automated optimal ordering of parameters for a general block of photographs, which may contain cross-flight strips, is a topic of current research (Lucas, 1981). Note that for a large block of photos, the off-diagonal portion N_{12} is very sparse.
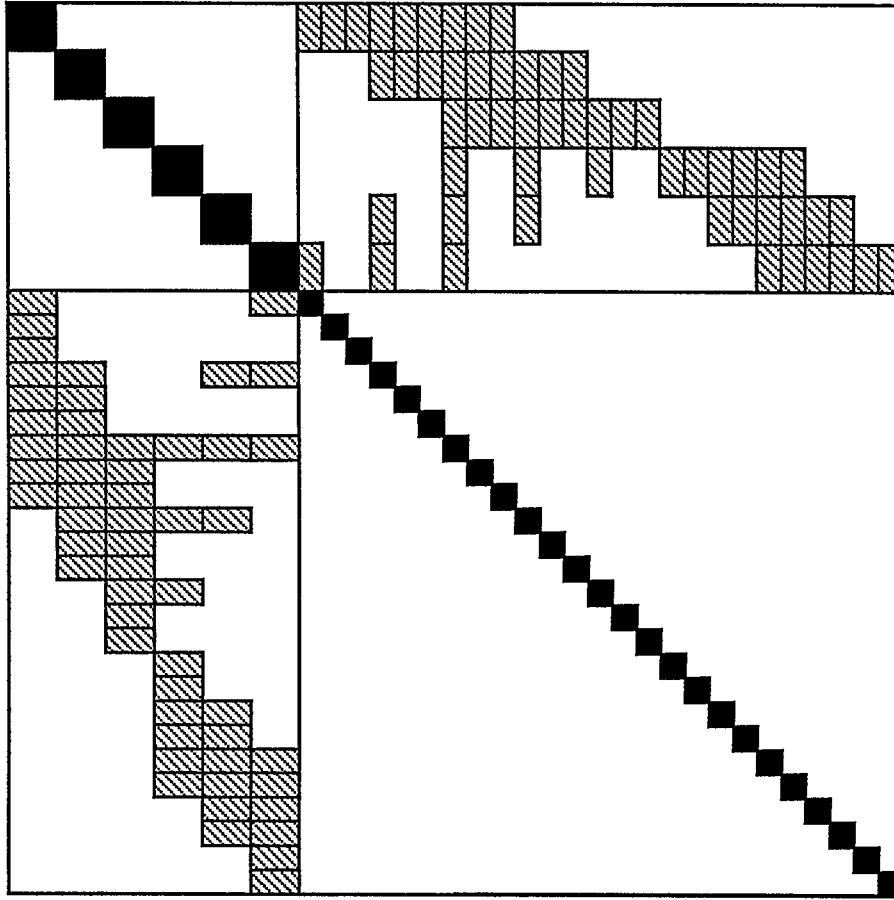
Figure 6.3.   Structure of normal equations

For the computation of (6.3) a simple matrix identity was used which relates the inverse of the normal coefficient matrix N to the terms in the partition (6.4):

$$N^{-1} = \begin{bmatrix} E & F \\ G & H \end{bmatrix} \quad (6.5a)$$

where

$$E = \left(N_{11} - N_{12} \cdot N_{22}^{-1} \cdot N_{12}^{T} \right)^{-1} \quad (6.5b)$$

$$G = -N_{22}^{-1} \cdot N_{12}^{T} \cdot E \tag{6.5c}$$

$$F = G^{T}, \text{ and} \tag{6.5d}$$

$$H = N_{22}^{-1} - N_{22}^{-1} \cdot N_{12}^{T} \cdot F \tag{6.5e}$$

(Faddeev and Faddeeva, 1963). Note that the largest submatrix to be inverted, N_{22}, is block diagonal with 3×3 blocks. Therefore, the inversion of N_{22} is accomplished by n 3×3 inversions, where n is the number of tie points. The off-diagonal submatrices are essentially folded into N_{11}, which is $6m \times 6m$, where m is the number of photos and $6m < 3n$. There are analogous formulae for the inversion of N for the case where $6m > 3n$ (ibid.). Brown (1976) describes more efficient methods in which formulae similar to (6.5) are applied recursively. These latter methods are also useful when parameters of self-calibration are added to the border of N. The more efficient partitioning schemes were not used in this investigation.

6.3 Simulation Results

An existing bundle adjustment program, written by M.A. Chapman, was modified for this investigation. These modifications were necessary to allow the adjustment of a reasonably-sized block ($\sim$ 50 photos) and to allow the introduction of covariances between coordinates for each exposure station. It was found that the "very large array" option on the Honeywell Multics computer was not sufficient for the former purpose (due to system bugs), so the program was modified to utilize disk input and output during processing of the normal equations. Packed storage

89

was also used to exploit the block-diagonal structure and symmetry of the coefficient matrix.

<u>Photography</u>

camera principal distance	...6 inches (152.4 mm)
camera format	...9 inches (228.6 mm)
average photo scale	...1 : 50 000
end lap	...60%
side lap	...30%
number of strips	...4
number of photos per strip	...12
number of tie points	...108
gimbal angle generation	...σ_ω, $\sigma_\phi = 3°$; $\sigma_\kappa = 5°$, random per photo
photocoordinate perturbations	...8 μm (1 σ)

<u>Interior Orientation Element Perturbations</u>

principal distance	...50 μm (1 σ), applied as bias
principal point offsets	...5 μm (1 σ), applied as bias

<u>Weights for Bundle Adjustment</u>

photocoordinate measurements	...1 / (8 μm)^2
exposure station coordinates	...as computed (see Chapter 4)
gimbal angles	...correspond to 1 / (10°)^2

Table 6.1.   Photogrammetric simulation summary

Table 6.1 summarizes the parameters of the photogrammetric simulation. The seven flight lines generated in the simulation were trimmed to four lines of 12 photos per line, for a total of 48 photos. The tie point configuration used is shown in Figure 6.4. The small squares are tie points near the principal points in each

photo. The terms Δh and $-\Delta h$ appearing in the figure refer to the simulated terrain variations; a value of 300 metres was used, but this is inconsequential in this context.
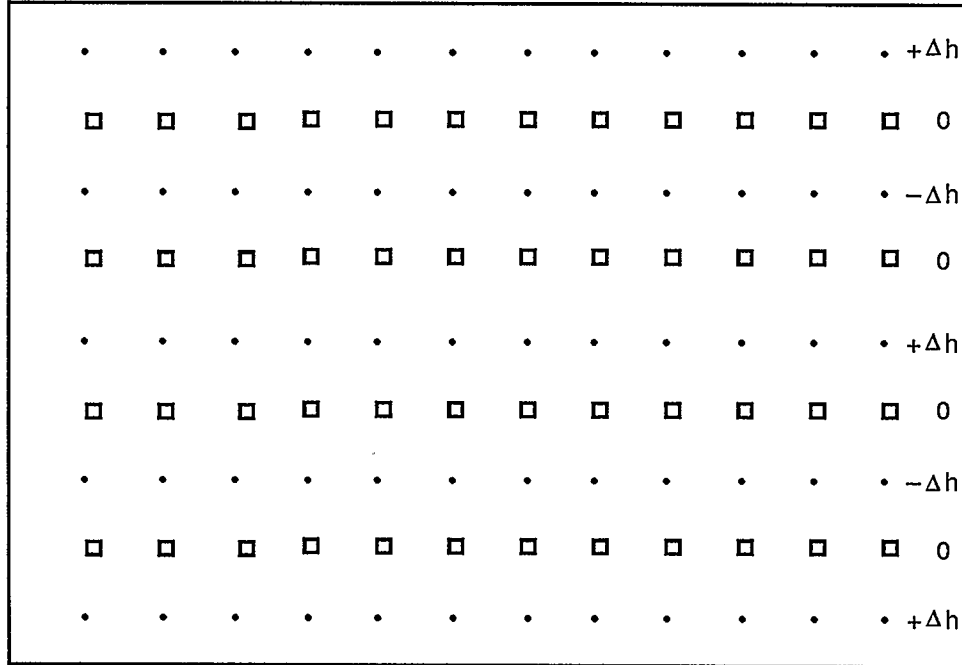
Figure 6.4.   Simulated tie points

The perturbations on the photocoordinate observations (8 μm, 1σ) are larger than usual; other investigators typically use 3 μm. As was mentioned in Chapter 5, the large value was used because it has been assumed that the points have not been pre-targetted. Pre-targetting of the points would increase the precision, but can be difficult and costly. If a subset of the points were to be pre-targetted, these points could be controlled using differential GPS observations

9 1

without significant additional effort, further enhancing the accuracy and reliability of the aerotriangulation.

Again, note that the weights used for the gimbal angles and the tie point ground coordinates are relatively small. Attitude information from the INS was not used in the bundle adjustment. Due to the high inherent geometric strength of photogrammetric blocks, accuracies of approximately 10 arc seconds or better are needed if such attitude information is to contribute to the adjustment (Schwarz et al., 1984). The best that can be expected of commercially-available stable-platform INS's is approximately 20-30 arc seconds. It should be mentioned, however, that auxiliary attitude information **is necessary** if only a single strip is to be adjusted, due to the indeterminancy of the gimbal angle ω in this situation. Also note that the gimbal angles obtained from the INS will be used to recover the orientations of the predetermined offset vectors between the GPS phase centre, INS reference centre, and camera perspective centre. Assuming the INS orientation angles are accurate within 1 arc minute, and assuming that the magnitude of these vectors is less than 5 metres, uncertainties of less than 2 millimetres will result in the exposure station coordinates. Therefore, these errors have not been explicitly simulated.

The aerotriangulation simulation results are summarized in Table 6.2. Each table entry is an average derived from five simulation runs. The values are rms differences between tie point coordinates obtained by aerotriangulation and their simulated true values. They are expressed in the local ground coordinate system in order ^Gx, ^Gy, ^Gz. The figures in parentheses in the last column are rms of ^Gz coordinate differences after the mean differences in each run have been removed, and are thus measures of the internal consistency of the ^Gz determination. Simulations for the entries which are left blank in the table were not carried out; they

Errors Positioning Strategy	image coordinates only	image coordinates + principal distance	all errors
I (GPS code + stable-platform INS)	—	—	0.49 0.69 2.59 (0.91)
II (GPS phase + strapdown INS)	0.45 0.55 0.84	0.45 0.55 1.86	0.47 0.58 1.87 (0.85)

Table 6.2.   Photogrammetric simulation results (rms, m)

would not contribute additional insight into the results.

It is apparent that of the three interior orientation elements which were perturbed, only the variations of the principal distance significantly affected the results. Uncertainties in the principal point offsets had negligible effects because of the inherent symmetry of the aerotriangulation, and because the perturbations were below the noise level of the photocoordinate measurements. Variations of the principal distance, however, do pose a significant problem. As indicated by the values in parentheses and by the last value in the first column, however, a good deal of the error is in the form of a bias. This assumes, of course, that the principal distance remains stable during the photography.

In general, the simulation results meet Class "A" map accuracy standards for scales of 1: 50 000 or smaller, as specified by the Canadian Surveys and Mapping Branch (Chapman, 1986). These standards call for standard errors of 2.33 metres in G_x and G_y and 2.43 metres in G_z. However, because the G_z

component of the simulated errors is largely a bias, these results may be adequate for mapping at even larger scales. For example, Class "A" standards for scales of 1: 20 000 call for standard errors of 0.93 metres in ^Gx and ^Gy , and 0.97 metres in ^Gz. Most applications of topographic maps require high relative accuracy; high absolute accuracy is less important. In practice, height biases are common in topographic maps. Furthermore, if the maps are maintained in a digital data base, such a bias can be easily corrected at a later date. Therefore, the techniques proposed in this thesis are sufficient for map scales as large as 1: 20 000 for many applications.

Note that Ackermann (1986) is much more optimistic about the prospects of photogrammetry without ground control.

Chapter 7

Conclusions and Recommendations

The simulations which were performed lead to the following conclusions:

1. Aircraft positions with half-metre accuracies are obtainable using either of the strategies outlined in this thesis.

2. Aerotriangulation simulations using these data have demonstrated that these positions are adequate as exclusive control for mapping at scales of 1: 50 000.

3. A height bias is present in the aerotriangulated points due to uncertainty in the cameras effective precalibrated principal distance. If this bias can be tolerated or eliminated, the results may be suitable for mapping at scales up to 1: 20 000.

The following recommendations are made:

1. For higher aerotriangulation accuracy, some form of in-flight camera calibration is needed. Self calibration of the primary elements of interior orientation is usually not possible with vertical photography over flat terrain due to projective coupling. Such calibration could be made possible, however, by photographing a control field near the airport before and after the mapping mission, by using photography taken during aircraft rolling maneuvers (Brown, 1985) in addition to

the vertical photography, by including photography taken over terrain which has large height variations (Merchant, 1973), or by using ground clearance measurements. Accuracy and reliability can also be enhanced by increasing side lap, by adding a few ground control points, or by pre-targetting some of the tie points.

2. The fact that the major observations in the aerotriangulation in this study are of two distinct types - perspective centre coordinates and photocoordinate observations - suggests that *variance component analysis* may be applicable. Here, the a posteriori variance of unit weight is decomposed into components which correspond to contributions from the distinct observation types. If the relative weights between these observation types have been entered incorrectly, variance components can then be used to rescale these weights (Mackenzie, 1985).

3. For aerotriangulation in production mapping, an efficient bundle adjustment program is needed. Such a program should use ideas outlined in Brown (1976). Furthermore, as computer power increases, the combined adjustment of photogrammetric and positioning data (ibid.; Anderson, 1985) becomes feasible.

The aircraft positioning techniques described here are applicable to other tasks in addition to aerotriangulation, such as airborne gravimetry and laser profiling. Simulations are only the first step in testing the proposed methods; field trials must follow. Recent tests using GPS phase data (Schwarz et al., 1987) have verified the simulation results, and have confirmed the need for cycle-slip control. Aerotriangulation tests are planned.

References

Ackermann, F. Joint photogrammetric block adjustment with navigation data as additional observations. *Minutes of the Joint Workshop on Combined Adjustment of Heterogeneous Geodetic and Photogrammetric Data*, University of Federal Armed Forces, Munich, September 1986.

American Society of Photogrammetry (ASP). *The Manual of Photogrammetry, Fourth Edition*, Falls Church, VA, 1980.

Anderson, J.M. A combined photogrammetric and Doppler adjustment. *Photogrammetric Engineering and Remote Sensing, 51(6)*, 655-666, June 1985.

Bate, R.R., D.D. Mueller, and J.E. White. *Fundamentals of Astrodynamics*, Dover, N.Y., 1971.

Bender, L.U. Analytical photogrammetry: a collinear theory. *Department of Geodetic Science Report No. 154*, The Ohio State University, Columbus, 1971.

Beser, J. and B.W. Parkinson. The application of NAVSTAR differential GPS in the civilian community. *Global Positioning System, 2*, 167-196, The Institute of Navigation, Washington, 1984.

Blais, J.A.R. Least-squares block adjustment of stereoscopic models and error analysis. *Department of Surveying Engineering Publication 30001*, The University of Calgary, 1979.

Blais, J.A.R. and M.A. Chapman. Optimal use of auxiliary airborne inertial data in topographical mapping applications. In K.P. Schwarz, ed., *Proceedings of the Third International Symposium on Inertial Technology for Surveying and Geodesy, 1*, 359-373, Banff, 1985.

Bletzacker, F.R. Reduction of multipath contamination in a geodetic GPS receiver. *Proceedings of the First International Symposium on Precise Positioning with the Global Positioning System, 1*, 413-422, U.S. NOAA, NGS, Rockville, Md., 1985.

Britting, K.R. *Inertial Navigation System Analysis*. Wiley-Interscience, New York, 1971.

Brown, D.C. The bundle adjustment - progress and prospects. Invited paper, Commission 3, 13th Congress of the International Society of Photogrammetry, Helsinki, 1976.

Brown, D.C. Personal communication, April 1985.

Brown, R.G. and P.Y.C. Hwang. A Kalman filter approach to precision GPS geodesy. *Global Positioning System, 2*, 155-166, The Institute of Navigation, Washington, 1984.

Buffett, B.A. A short-arc orbit determination for the Global Positioning System. M.Sc. Thesis, *Department of Surveying Engineering Publication 20013*, The University of Calgary, 1985.

Cannon, M.E. Kinematic positioning using GPS pseudorange and carrier phase observations. M.Sc. Thesis, *Department of Surveying Engineering Publication 20019*, The University of Calgary, 1987.

Chapman, M.A. Course lecture notes, Photogrammetric Mapping, Dept. of Surveying Engineeing The Universtity of Calgary, 1986.

Chapman, M.A. Personal communication, July 1987.

Corten, F.L.J.H. Applications of navigation systems and of sensor orientation systems in survey navigation, in aerial triangulation, and establishment of control. *International Archives of Photogrammetry and Remote Sensing*, Rio de Janeiro, 16-29 June 1984.

Counselman, C.C. and I.I. Shapiro. Miniature interferometric terminals for earth surveying. *Bulletin Geodesique*, *53*, 139-163, 1979.

Decker, B.L. World Geodetic System 1984. *Proceedings of the Fourth International Geodetic Symposium on Satellite Positioning*, *1*, 69-92 Austin, Texas, April-May 1986.

Denaro, R.P. Simulation and analysis of differential GPS. *Proceedings of the National Technical Meeting of the Institute of Navigation*, San Diego, 1984.

Divine, D. and S.G. Francisco. Synchromesh, a practical enhancement to GPS service. *IEEE PLANS '84 Record*, 169-174, San Diego, November 1984.

Faddeev, D.K. and V.N. Faddeeva. *Computational Methods of Linear Algebra*, W.H. Freeman, San Fransico, 1963.

Fell, P.J. Geodetic positioning using a Global Positioning System of satellites. *Department of Geodetic Science Report No. 299*, The Ohio State University, Columbus, 1980.

Fryer, J.G. and D.C. Brown. Lens distortion for close range photogrammetry. *Photogrammetric Engineering and Remote Sensing*, *52(1)*, 51-58, January 1986.

Fullenwider, E.D. and P.S. Jorgensen. The updated NAVSTAR/GPS test and operational constellations. *IEEE Position Location and Navigation Symposium Record*, 315-320, San Diego, 1984.

Gelb, A., ed. *Applied Optimal Estimation*, The M.I.T. Press, 1974.

Goldfarb, J.M. and K.P. Schwarz. Kinematic positioning with an integrated INS-differential GPS. *Proceedings of the First International Symposium on Precise Positioning with the Global Positioning System*, 2, 757-772, U.S. NOAA, NGS, Rockville, Md., 1985.

Hatch, R. The synergism of GPS code and carrier measurements. *Magnavox Technical Paper MX-TM-3353-82*, Magnavox Advanced Products and Systems Company, Torrance, CA, January 1987

Heiskanen, W.A. and H. Moritz. *Physical Geodesy*, W.H. Freeman, San Francisco, 1967.

Kalafus, R.M., J. Vilcans, and N. Knable. Differential operation of NAVSTAR GPS. *Global Positioning System*, 2, 197-214, The Institute of Navigation, Washington, 1984.

Kok, A.L. Preprocessing and filtering of digitally correlated Gestalt data. M.Sc. Thesis, *Department of Surveying Engineering Publication 20016*, The University of Calgary, 1986.

Krakiwsky, E.J. A synthesis of recent advances in the method of least squares. *Department of Surveying Engineering Publication 10003*, The University of Calgary, 1982.

Krakiwsky, E.J., D.B. Thomson, and R.R. Steeves. A manual for geodetic coordinate transformations in the Maritimes. *Department of Surveying Engineering Technical Report No. 48*, The University of New Brunswick, Fredericton, 1977.

Krakiwsky, E.J., B. Wanless, B. Buffet, K.P. Schwarz, and M. Nakiboglu. GPS orbit improvement and precise positioning. *Proceedings of the First International Symposium on Precise Positioning with the Global Positioning System*, 1, 73-86, U.S. NOAA, NGS, Rockville, Md., 1985.

Lachapelle, G., J. Lethaby, and M. Casey. Airborne single point and differential GPS navigation for hydrographic bathymetry. *The Hydrographic Journal*, 34, October 1984.

Lucas, J.R. Results of photogrammetric control densification in Ada County, Idaho. *NOAA Technical Report NOS 91 NGS 21*, U.S. Department of Commerce, December 1981.

Lucas, J.R. Photogrammetric densification of control in Ada County, Idaho: data processing and results. *Photogrammetric Engineering and Remote Sensing*, 50(5), 569-575, May 1984.

Lucas, J.R. Aerotriangulation without ground control. *Photogrammetric Engineering and Remote Sensing*, 53(3), 311-314, March 1987.

MacDoran, P.F. Satellite emission radio interferometric earth surveying, SERIES-GPS geodetic system. *Bulletin Geodesique, 53*, 117-138, 1979.

Mackenzie, A.P. Design and assessment of horizontal survey networks. M.Sc. Thesis, *Department of Surveying Engineering Publication 20011*, The University of Calgary, 1985.

Mader, G.L. Dynamic positioning using GPS carrier phase measurements. *Manuscipta Geodaetica, 11(4)*, 1986.

Martin, E.H. GPS user equipment error models. *Global Positioning System*, 109-118, The Institute of Navigation, Washington, 1980.

Merchant, D.C. Elements of photogrammetry. Lecture notes, Department of Geodetic Science, The Ohio State University, Columbus, 1973.

Mikhail, E.M. *Observations and Least Squares*, University Press, Washington, 1976.

Milliken, R.J. and C.J. Zoller. Principle of operation of NAVSTAR and system characteristics. *Global Positioning System*, 3-14, The Institute of Navigation, Washington, 1980.

Moritz, H. Inertia and gravitation in geodesy. Keynote address in K.P. Schwarz, ed., *Proceedings of the Third International Symposium on Inertial Technology for Surveying and Geodesy*, 1, 1-8, Banff, 1985.

Mueller, I.I. *Spherical and Practical Astronomy as Applied to Geodesy*, Frederick Ungar, N.Y., 1969.

Munjy, R.A.H. Self calibration using the finite element approach. *Photogrammetric Engineering and Remote Sensing, 52(3)*, 411-418, March 1986.

Payne, C.R. NAVSTAR Global Positioning System. *Proceedings of the Third International Symposium on Satellite Doppler Positioning*, 993-1021, Las Cruces, NM, 1982.

Rauhala, U.A. Fast compiler positioning algorithms and techniques of array algebra in analytical and digital photogrammetry. Paper presented at the Intercommission Conference of the International Society of Photogrammetry and Remote Sensing, Interlaken, Switzerland, June 1987.

Remondi, B.W. Using the Global Positioning System (GPS) phase observable for relative geodesy: modeling, processing, and results. *NOAA Reprint*, U.S. Department of Commerce, Rockville, MD, 1984.

Schwarz, K.P. Inertial adjustment models - a study of some underlying assumtions. In K.P. Schwarz and G. Lachapelle, editors, *Geodesy in Transition*, Department of Surveying Engineering, The University of Calgary, 1983a.

Schwarz, K.P. Inertial surveying and geodesy. *Reviews of Geophysics and Space Physics, 21(4),* 878-890, May 1983b.

Schwarz, K.P. Course lecture notes, Space and Inertial Positioning, Dept. of Surveying Engineeing The Universtity of Calgary, 1985a.

Schwarz, K.P. A unified approach to post mission processing of inertial data. *Bulletin Geodesique, 59(1),* 1985b.

Schwarz, K.P., M.E. Cannon, and R.V.C. Wong. The use of GPS in exploration geophysics. Paper presented at the XIX General Meeting of the IUGG, Vancouver, Canada, August 1987.

Schwarz, K.P., C.S. Fraser, and P.C. Gustafson. Aerotriangulation without ground control. *International Archives of Photogrammetry and Remote Sensing, 25, Part A1,* Rio de Janeiro, 16-29 June 1984.

Spilker, J.J. Signal structure and performance characteristics. *Global Positioning System,* 29-54, The Institute of Navigation, Washington, 1980.

Swift, E.R. NSWC's GPS orbit / clock determination system. *Proceedings of the First International Symposium on Precise Positioning with the Global Positioning System, 1,* 51-62, U.S. NOAA, NGS, Rockville, Md., 1985.

VanBronkhorst, A. Strapdown system algorithms. *NATO AGARD Lecture Series No. 95,* Neuilly Sur Seine, France, 1978.

Van Dierendonck, A.J., S.S. Russell, E.R. Kopitzke, and M. Birnbaum. The GPS navigation message. *Global Positioning System,* 55-73, The Institute of Navigation, Washington, 1980.

Vanicek, P. and E.J. Krakiwsky. *Geodesy: The Concepts, Second Edition,* North-Holland, Amsterdam, 1986.

Vanicek, P., R. Langley, D.E. Wells, and D. Delikaraoglou. Geometrical aspects of differential GPS postioning. *Bulletin Geodesique, 58,* 37-52, 1984.

Vassiliou, A. Processing of unfiltered inertial data. M.Sc. Thesis, *Department of Surveying Engineering Publication 20006,* The University of Calgary, 1984.

Wanless, B.A. Personal communication, June 1987.

Wolf, P.R. *Elements of Photogrammetry,* McGraw-Hill, N.Y., 1974.

Wong, R.V.C. A Kalman filter-smoother for an inertial survey system of the local level type. M.Sc. Thesis, *Department of Surveying Engineering Publication 20001,* The University of Calgary, 1982.

101

Wong, R.V.C. and K.P. Schwarz. Dynamic positioning with an integrated GPS-INS: formulae and baseline tests. *Department of Surveying Engineering Publication 30003*, The University of Calgary, 1983.

Appendix

Derivation of the Velocity Rate Equation in the Local Level Frame

Applying equation (3.13) to the transformation from the operational inertial frame to the conventional terrestrial frame, and using (3.12b)

$$^{LL}\mathbf{v} = {}^{LL}\mathbf{R}_{CT} \cdot {}^{CT}\mathbf{R}_I \cdot ({}^I\Omega_{CTI} \cdot {}^I\mathbf{r} + {}^I\dot{\mathbf{r}}) = {}^{LL}\mathbf{R}_I \cdot ({}^I\dot{\mathbf{r}} - {}^I\Omega_{ICT} \cdot {}^I\mathbf{r}). \qquad \text{(A.1)}$$

Differentiating (A.1)

$$^{LL}\dot{\mathbf{v}} = {}^{LL}\mathbf{R}_I \cdot {}^I\Omega_{LLI} \cdot ({}^I\dot{\mathbf{r}} - {}^I\Omega_{ICT} \cdot {}^I\mathbf{r})$$

$$+ {}^{LL}\mathbf{R}_I \cdot ({}^I\ddot{\mathbf{r}} - {}^I\dot{\Omega}_{ICT} \cdot {}^I\mathbf{r} - {}^I\Omega_{ICT} \cdot {}^I\dot{\mathbf{r}}). \qquad \text{(A.2)}$$

In substituting GMST for GAST in equation (3.5), the earth's rotation rate has been assumed to be constant, i.e.

$$^I\dot{\Omega}_{ICT} \equiv 0. \qquad \text{(A.3)}$$

Therefore,

$$^{LL}\dot{\mathbf{v}} = {}^{LL}\mathbf{R}_I \cdot [{}^I\ddot{\mathbf{r}} + ({}^I\Omega_{LLI} - {}^I\Omega_{ICT}) \cdot {}^I\dot{\mathbf{r}} - {}^I\Omega_{LLI} \cdot {}^I\Omega_{ICT} \cdot {}^I\mathbf{r}]. \qquad \text{(A.4)}$$

Decomposing $^I\Omega_{LLI}$ (Britting, 1971), and using (3.12b)

$$^I\Omega_{LLI} = {}^I\Omega_{LLCT} + {}^I\Omega_{CTI} = {}^I\Omega_{CTI} - {}^I\Omega_{CTLL}. \qquad \text{(A.5)}$$

Thus

$$^{LL}\mathbf{v} = {}^{LL}\mathbf{R}_I \cdot [{}^I\dot{\mathbf{r}} + ({}^I\Omega_{CTI} - {}^I\Omega_{CTLL} - {}^I\Omega_{ICT}) \cdot {}^I\dot{\mathbf{r}}$$

$$- ({}^I\Omega_{CTI} - {}^I\Omega_{CTLL}) \cdot {}^I\Omega_{ICT} \cdot {}^I\mathbf{r}] . \quad (A.6)$$

From (3.12b)

$$^{LL}\mathbf{v} = {}^{LL}\mathbf{R}_I \cdot [{}^I\ddot{\mathbf{r}} - ({}^I\Omega_{CTLL} + 2{}^I\Omega_{ICT}) \cdot {}^I\dot{\mathbf{r}} + ({}^I\Omega_{ICT} + {}^I\Omega_{CTLL}) \cdot {}^I\Omega_{ICT} \cdot {}^I\mathbf{r}].$$

$$(A.7)$$

Applying (3.13) and decomposing $^I\Omega_{CTLL}$,

$$^{LL}\dot{\mathbf{v}} = {}^{LL}\mathbf{R}_I \cdot [{}^I\ddot{\mathbf{r}} - ({}^I\Omega_{CTLL} + 2{}^I\Omega_{ICT}) \cdot {}^I\mathbf{R}_{LL} \cdot ({}^{LL}\dot{\mathbf{r}} + {}^{LL}\Omega_{ILL} \cdot {}^{LL}\mathbf{r}) \cdot$$

$$+ ({}^I\Omega_{ICT} + {}^I\Omega_{CTLL}) \cdot {}^I\Omega_{ICT} \cdot {}^I\mathbf{r}]$$

$$= {}^{LL}\mathbf{R}_I \cdot [{}^I\ddot{\mathbf{r}} - ({}^I\Omega_{CTLL} + 2{}^I\Omega_{ICT}) \cdot {}^I\mathbf{R}_{LL} \cdot ({}^{LL}\dot{\mathbf{r}} + {}^{LL}\Omega_{ICT} \cdot {}^{LL}\mathbf{r}$$

$$+ {}^{LL}\Omega_{CTLL} \cdot {}^{LL}\mathbf{r}) + ({}^I\Omega_{ICT} + {}^I\Omega_{CTLL}) \cdot {}^I\Omega_{ICT} \cdot {}^I\mathbf{r}] \quad (A.8)$$

From (3.13), equation (3.15) may be transformed as follows

$$^{LL}\mathbf{v} = {}^{LL}\mathbf{R}_{CT} \cdot [{}^{CT}\mathbf{R}_{LL} \cdot ({}^{LL}\dot{\mathbf{r}} + {}^{LL}\Omega_{CTLL} \cdot {}^{LL}\mathbf{r})]$$

$$= {}^{LL}\dot{\mathbf{r}} + {}^{LL}\Omega_{CTLL} \cdot {}^{LL}\mathbf{r} . \quad (A.9)$$

104

Using this result in (A.8) and substituting $^I\mathbf{R}_{LL} \cdot {}^{LL}\mathbf{r}$ for $^I\mathbf{r}$

$$
\begin{aligned}
{}^{LL}\dot{\mathbf{v}} = {}^{LL}\mathbf{R}_I \cdot [\,{}^I\ddot{\mathbf{r}} &- ({}^I\Omega_{CTLL} + 2{}^I\Omega_{ICT}) \cdot {}^I\mathbf{R}_{LL} \cdot {}^{LL}\mathbf{v} \\
&- ({}^I\Omega_{CTLL} + 2{}^I\Omega_{ICT}) \cdot {}^I\mathbf{R}_{LL} \cdot {}^{LL}\Omega_{ICT} \cdot {}^{LL}\mathbf{r} \\
&+ ({}^I\Omega_{ICT} + {}^I\Omega_{CTLL}) \cdot {}^I\Omega_{ICT} \cdot {}^I\mathbf{R}_{LL} \cdot {}^{LL}\mathbf{r}\,]
\end{aligned}
\tag{A.10}
$$

Noting that skew-symmetric matrices transform under similarities (ibid.), as do products of skew-symmetric matrices, i.e.

$$
{}^j\Omega_{ji} = {}^j\mathbf{R}_i \cdot {}^i\Omega_{ji} \cdot {}^i\mathbf{R}_j
\tag{A.11a}
$$

$$
\begin{aligned}
{}^j\Omega_{ji} \cdot {}^j\Omega_{ji} &= ({}^j\mathbf{R}_i \cdot {}^i\Omega_{ji} \cdot {}^i\mathbf{R}_j) \cdot ({}^j\mathbf{R}_i \cdot {}^i\Omega_{ji} \cdot {}^i\mathbf{R}_j) \\
&= {}^j\mathbf{R}_i \cdot {}^i\Omega_{ji} \cdot {}^i\Omega_{ji} \cdot {}^i\mathbf{R}_j,
\end{aligned}
\tag{A.11b}
$$

equation (A.10) becomes

$$
\begin{aligned}
{}^{LL}\dot{\mathbf{v}} &= {}^{LL}\mathbf{R}_I \cdot {}^I\ddot{\mathbf{r}} - ({}^{LL}\Omega_{CTLL} + 2{}^{LL}\Omega_{ICT}) \cdot {}^{LL}\mathbf{v} \\
&\quad - ({}^{LL}\Omega_{CTLL} + 2{}^{LL}\Omega_{ICT}) \cdot {}^{LL}\Omega_{ICT} \cdot {}^{LL}\mathbf{r} \\
&\quad + ({}^{LL}\Omega_{ICT} + {}^{LL}\Omega_{CTLL}) \cdot {}^{LL}\Omega_{ICT} \cdot {}^{LL}\mathbf{r} \\
&= {}^{LL}\mathbf{R}_I \cdot {}^I\ddot{\mathbf{r}} - ({}^{LL}\Omega_{CTLL} + 2{}^{LL}\Omega_{ICT}) \cdot {}^{LL}\mathbf{v} - {}^{LL}\Omega_{ICT} \cdot {}^{LL}\Omega_{ICT} \cdot {}^{LL}\mathbf{r}
\end{aligned}
\tag{A.12}
$$

which is the relation required for the mechanization equation.